

Partial recovery of meter-scale surface weather

Jonathan Giezendanner^{1*}, Qidong Yang¹, Eric Schmitt²,
Anirban Chandra², Daniel Salles Civitarese³, Johannes Jakubik³,
Jeremy Vila², Detlef Hohl², Campbell Watson³, Sherrie Wang^{1*}

¹MIT.

²Shell Information Technology International Inc.

³IBM.

*Corresponding author(s). E-mail(s): {[jgiezend](mailto:jgiezend@mit.edu), [sherwang](mailto:sherwang@mit.edu)}@mit.edu;

Abstract

Near-surface atmospheric conditions can differ sharply over tens to hundreds of meters due to land cover and topography, yet this variability is absent from current weather analyses and forecasts. It is unclear whether such meter-scale variability reflects irreducibly chaotic dynamics or contains a component predictable from surface characteristics and large-scale atmospheric forcing. Here we show that a substantial, physically coherent component of meter-scale near-surface weather is statistically recoverable from existing observations. By conditioning coarse atmospheric state on sparse surface station measurements and high-resolution Earth observation data, we infer spatially continuous fields of near-surface wind, temperature, and humidity at 10 m resolution across the contiguous United States. Relative to ERA5, the inferred fields reduce wind error by 29% and temperature and dewpoint error by 6%, while explaining substantially more spatial variance at fixed time steps. They also exhibit physically interpretable structure, including urban heat islands, evapotranspiration-driven humidity contrasts, and wind speed differences across land cover types. Our findings expand the frontier of weather modeling by demonstrating a computationally feasible approach to continental-scale meter-resolution inference. More broadly, they illustrate how conditioning coarse dynamical models on static fine-scale features can reveal previously unresolved components of the Earth system.

Keywords: Earth Observation, Weather, Near-surface meteorology, Machine learning

Weather at the Earth’s surface can change across meter scales: think of stepping from a shaded park into a sunlit street or breaking above the treeline into exposed wind. These small-scale variations — which we here refer to as “micro-weather” — are created by terrain, vegetation, buildings, and other surface features, and in turn impact human heat exposure [1, 2], renewable energy performance [3], wildfire propagation [4, 5], and pollutant dispersion [6]. Despite their importance, micro-weather variations are not captured by numerical weather predictions (NWP) and reanalysis products at regional or global scales [7–11], since NWP, along with their recent machine-learning emulators [12–19], are run at grid spacings of several kilometers. This coarse spatial resolution is likely to persist for some time as models continue to contend with computational limits and the breakdown of parameterizations at high resolution [20–22]. At the time of writing, for example, the emerging digital twin initiative at ECMWF aims to simulate the atmosphere at ~ 1 km resolution [22, 23].

Prior pathways to resolving weather at sub-kilometer scales have mainly involved running large eddy simulations to model convection and boundary layer processes [24–26]. But doing so at the scale of continents or the globe remains computationally infeasible. Meanwhile, statistical methods have downscaled atmospheric fields to ~ 1 km [27], but it remains unclear whether meter-scale variability can be recovered from existing observations. In this work, rather than resolve atmospheric dynamics at ever-higher resolutions, we test whether a component of micro-weather is predictable when coarse atmospheric dynamics are conditioned on static or slow-varying high-resolution Earth observation data. We refer to this component as the “statistically recoverable component of micro-weather”.

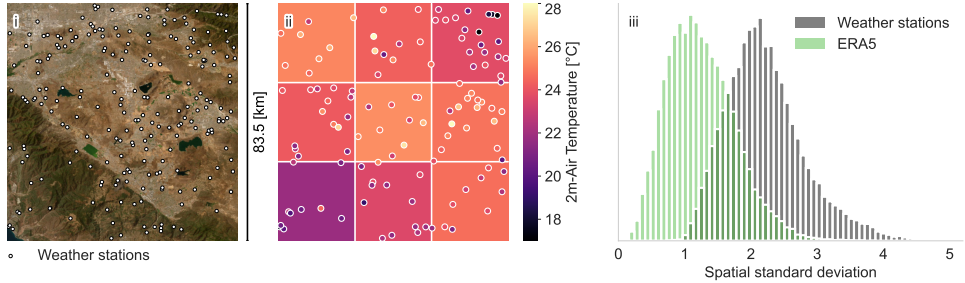
Our ability to address this question is enabled by the fact that Earth observation now resolves the land surface at meter to tens-of-meter resolution globally [28]. Although these images are static and therefore cannot encode dynamic information about the atmosphere, multispectral satellite imagery, land-cover classifications, and digital elevation models capture properties that shape micro-scale atmospheric behavior [29–31]. For example, wind must maneuver around terrain, vegetation has a cooling effect, and surface materials differ in moisture retention.

We show that a substantial portion of micro-weather is statistically recoverable by combining large-scale atmospheric forcing with static land surface characteristics. We train a multimodal deep learning model on ERA5 reanalysis and high-resolution satellite data to predict observations at 11,000 weather stations across the contiguous United States. Then, at inference time, we generate spatially continuous near-surface micro-weather fields at 10 m resolution. We evaluate against millions of held-out station observations and find that the inferred micro-weather fields both explain a larger fraction of spatial variation in weather and reduce the mean absolute error compared to ERA5 reanalysis. These improvements are stable across land cover types.

Despite being trained on sparse weather station measurements, the inferred fields also recover physically interpretable and coherent patterns at meter scales, including urban heat islands, temperature declines with elevation, wind channeling with terrain, and evapotranspiration-driven humidity gradients. Independent comparisons with land-surface temperature observations from the ECOSTRESS sensor lend further credence to the spatial structure of the inferred air temperature fields [32]. Together,

these results show that near-surface micro-weather contains a component that can be inferred from existing observations. More broadly, our work demonstrates how coarse dynamical models can be conditioned on fine-scale environmental structure to reveal previously unresolved variability.

a Kilometer-scale reanalysis does not resolve micro-weather variability



b Overview of our micro-weather framework

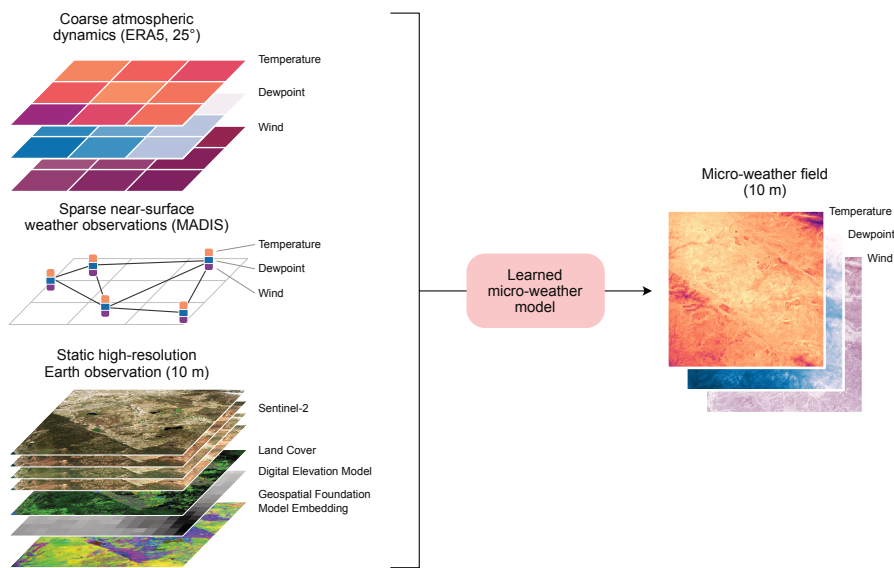


Fig. 1 Inference framework combining reanalysis, surface stations, and Earth observation to recover sub-kilometer weather variability. (a) (i) Example over the Los Angeles metropolitan area illustrating that kilometer-scale reanalysis (ERA5) does not resolve meter-scale weather variability. (ii) 2 m air temperature from ERA5 (grid) and as measured by surface weather stations (points). (iii) Histogram of the spatial standard deviation of 2 m air temperature (from 2020–2023) across the weather stations versus across the nine ERA5 grid cells. (b) Overview of the inference framework. The model combines coarse atmospheric dynamics from ERA5, observations from sparse surface stations, and high-resolution Earth observation data to generate spatially continuous 10 m resolution fields of 2 m air temperature, 2 m dewpoint temperature, and 10 m wind.

The micro-weather model

Our approach integrates three complementary sources of information to infer near-surface micro-weather (Figure 1). First, we use ERA5 reanalysis to represent the coarse-scale atmospheric state at $0.25^\circ \times 0.25^\circ$ spatial resolution and hourly temporal resolution. In particular, we provide the model with 10m wind u and v , 2m temperature, and 2m dewpoint temperature from ERA5 interpolated to the target location and locations of all weather stations. Second, we incorporate point-based weather observations from a backbone network of surface stations drawn from the NOAA Meteorological Assimilation Data Ingest System (MADIS). These observations provide accurate but spatially sparse measurements of near-surface conditions for the same variables of 10m wind, 2m temperature, and 2m dewpoint. Third, we use high-resolution Earth observation (EO) data — including multi-spectral satellite imagery, land-cover maps, and digital elevation models — to characterize fine-scale surface heterogeneity. In some experiments, our model directly learns how to make use of the EO data stack in an end-to-end fashion; in others, we use precomputed geospatial foundation model embeddings that summarize land-surface structure at 10 m resolution. These approaches achieve comparable accuracy in our experiments, and we henceforth report results for the best-performing configuration (i.e., AlphaEarth embeddings [33]).

To combine these different data modalities, we employ a deep learning model with a custom transformer architecture (Figure 1). Transformers are well-suited to this task because they can integrate information from multiple spatially distributed sources, learn interactions across different input types, and condition predictions at arbitrary target locations on a shared representation of atmospheric context [34]. In our formulation, the model distinguishes between two types of locations. At backbone weather station locations, the model has access to (i) the coarse atmospheric state from ERA5, (ii) observed near-surface weather variables from the station, and (iii) Earth observation features at the station location. At target locations, where no weather observations are assumed to be available, the model is provided only with the coarse atmospheric state and Earth observation features. All inputs are embedded into a common latent space together with geographic location information, allowing the model to learn spatial relationships among stations and between stations and target locations. Through attention mechanisms, the model learns how to weigh information from relevant backbone stations and the target location to infer weather at target locations, enabling inference of weather at high spatial resolution at locations between stations.

The model is trained in a supervised manner using hourly weather station observations from 2020–2023 as ground truth. Stations across the U.S. are partitioned into four disjoint sets with different roles (Figure 5): (1) 8,000 backbone stations provide information on nearby weather during training and inference, while 3,000 target stations are divided further into (2) training, (3) validation, and (4) test sets. During training, the model is optimized to predict weather at training stations, while validation stations are used to select model hyperparameters. Test stations are held out entirely and used exclusively for evaluation. Importantly, no weather observations from held-out stations are seen by the model at any time; predictions at test station locations rely solely on ERA5 and EO features at the target location and observations from

the backbone network. Model performance is assessed by comparing inferred values at held-out stations against their observed measurements. This experimental design ensures that performance gains reflect learned generalization across space and surface conditions.

Once trained, the model can be applied to infer near-surface weather variables at arbitrary locations and times by combining the coarse atmospheric state from ERA5 with Earth observation features at the target location and contextual information from the backbone station network. This enables the generation of spatially continuous micro-weather fields at 10 m resolution over large geographic domains. These inferred fields represent the statistically recoverable component of micro-weather conditioned on surface features and large-scale atmospheric forcing.

Accuracy assessment

Across the continental United States, our micro-weather fields consistently reduce near-surface weather error relative to ERA5 reanalysis. Averaged over all held-out test stations and timesteps, wind vector error is reduced by 29%, while mean absolute errors (MAE) in 2 m air temperature and 2 m dewpoint temperature are reduced by 6% compared to interpolated ERA5 (Figure 2a). These improvements are observed across a wide range of climatic regions and land cover types, with particularly large error reductions for wind in forested and built-up areas (Figure A3).

Error reductions also exhibit coherent regional structure. For temperature and dewpoint, improvements relative to ERA5 extend across the western, eastern, and mid-Atlantic United States, while performance is weaker in the northern Great Plains (Figure 2d). For wind, error reductions are more spatially extensive, with strong improvements across the Midwest and South as well; however, the northern Great Plains continue to see worse performance. Worse-performing regions appear to coincide with relatively sparse station coverage and more homogeneous surface characteristics at kilometer scales, which may reduce the amount of recoverable fine-scale structure given the available inputs.

To assess whether improvements arise from interpolation of station data alone or from learned integration of station and EO data, we compare the micro-weather model against two additional baselines: spatial interpolation of station observations and a model that combines ERA5 reanalysis with backbone station observations but excludes EO inputs. Station interpolation performs worse than ERA5 for temperature and dewpoint and yields only modest improvements for wind (4% reduction in error). In contrast, the model combining ERA5 and backbone stations without EO data already outperforms both ERA5-only and station-only baselines (Figure 2), reducing temperature error by 2.6% on average, dewpoint error by 1.0%, and wind error by 23%. The comparatively large reduction in wind error reflects, in part, a systematic high bias in ERA5 near-surface wind speeds, which is reduced by incorporating station observations.

Adding high-resolution EO data further improves performance. Compared to the ERA5 plus stations baseline, the full micro-weather model achieves additional error reductions for all variables (Figure 2). For temperature and dewpoint, improvements

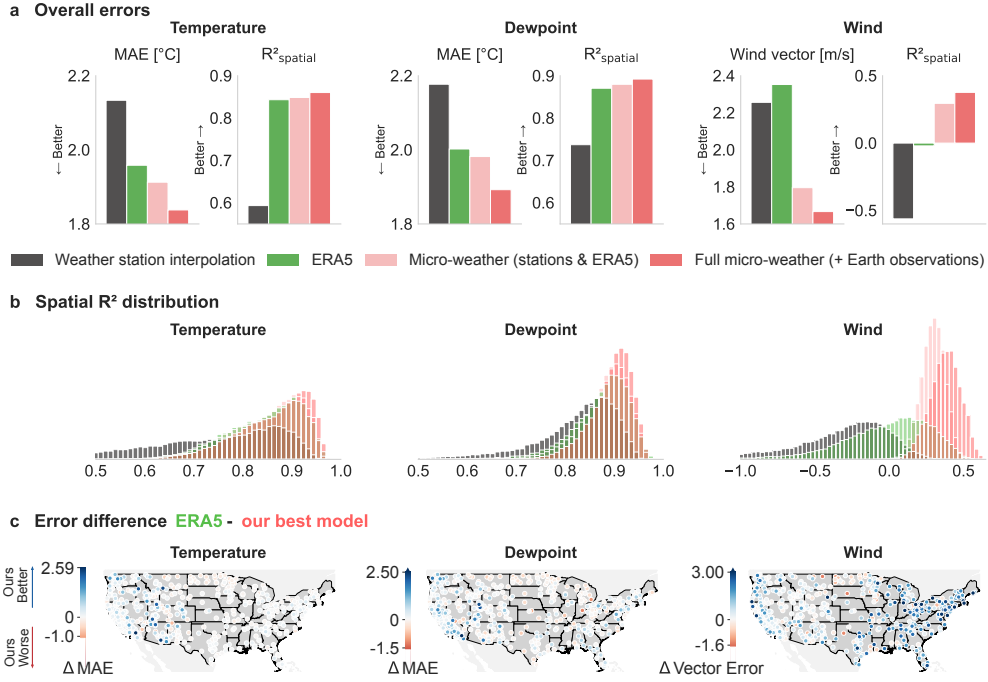


Fig. 2 Quantitative evaluation of inferred micro-weather fields relative to baseline methods. (a) Mean absolute error (MAE) or vector error and spatial coefficient of determination (R^2_{spatial} , de-meaned per timestep to isolate spatial variability) across all held-out test stations for temperature, dewpoint, and wind. Baselines include spatial interpolation of weather stations, ERA5 reanalysis, and a model using ERA5 and stations without Earth observation inputs. (b) Histograms of spatial R^2 values across hourly timesteps from 2020–2023, where each R^2_{spatial} is computed for one timestep across all held-out test stations. (c) Map of station-level error reduction relative to ERA5, defined as the difference between ERA5 error and full inference model error, averaged over 2020–2023. Positive values indicate improvement over ERA5.

from adding EO data (3.6% and 4.5% reduction in MAE, respectively) are greater in magnitude than those obtained by adding station data to ERA5. For wind, a large fraction of the total improvement arises from incorporating station observations, and EO provides a smaller additional contribution (6% further error reduction, for a total of 29% error reduction relative to ERA5). These results indicate that fine-scale surface information contributes additional, non-redundant skill beyond that provided by coarse atmospheric state and nearby observations.

While reductions in pointwise error indicate improved agreement with station observations, they do not by themselves establish that fine-scale spatial structure is being captured, as error reductions can arise from correcting mean biases in ERA5. Because micro-weather is defined by variability at scales unresolved by kilometer-scale models, we also evaluate the ability of the inferred fields to capture spatial variance relative to baseline methods. Using a de-meaned coefficient of determination that isolates spatial variability at fixed time steps (Methods), we find that the micro-weather

fields explain a significantly larger fraction of observed spatial variance than ERA5-only or station-only predictions for wind, temperature, and dewpoint (Figure 2a). This improvement in spatial variance explained is evident both at the national scale (Figure 2b) and within localized regions examined in our case studies (Figure 3), and is consistently observed across the study period (2020–2023).

Together, these results demonstrate that a substantial fraction of near-surface micro-scale weather variability is predictable from the available inputs. The inferred micro-weather fields capture variance that is absent from kilometer-scale reanalysis and cannot be recovered through station interpolation alone, motivating a closer examination of the physical structure of the recovered fields.

Physical structure recovery

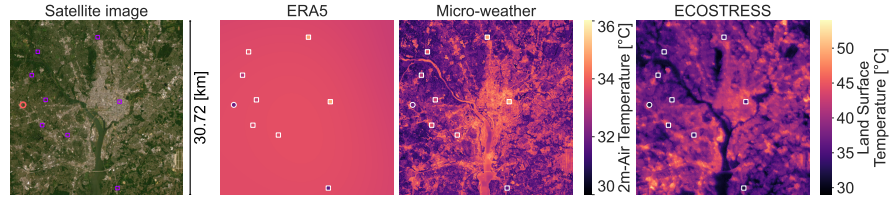
Beyond improving predictions at individual stations, the inferred micro-weather fields exhibit spatially coherent physical structure at meter scales. Figure 3 presents representative case studies illustrating the inferred micro-weather structure for near-surface temperature, dewpoint temperature, and wind. The baseline regional value is anchored to ERA5, while fine-scale variability is influenced by a combination of nearby backbone station measurements, land cover, and topography at scales of tens to hundreds of meters.

For temperature, the inferred fields recover urban heat islands, cooler conditions in forested and vegetated areas, and temperature gradients that vary with local topography. For instance, in the Washington, D.C. metropolitan area (Figure 3a), the micro-weather field predicts warmer air temperatures over dense built-up regions, intermediate temperatures in suburban areas with tree cover, and cooler temperatures in forested regions. Temperature contrasts between land cover types reach several degrees Celsius, comparable to differences observed between station measurements within the same region. (Because no weather stations are located over open water in our dataset, we do not interpret inferred temperature over the Potomac River.) In the complex terrain surrounding Mount Lemmon in Tucson, Arizona (Figure 3b), the inferred temperature field decreases with elevation over short horizontal distances. Although backbone stations are located at lower elevations, the model correctly predicts substantially cooler temperature at a held-out station near the mountain summit. Across temperature case studies, independent comparisons with ECOSTRESS land surface temperature (LST) observations show strong qualitative agreement in spatial structure. Given the high correlation between LST and 2 m air temperature — with daytime LST tending to be higher than air temperature under clear, low-wind conditions but very similar to it under windy conditions [35] — this agreement supports the physical plausibility of the inferred micro-scale structure.

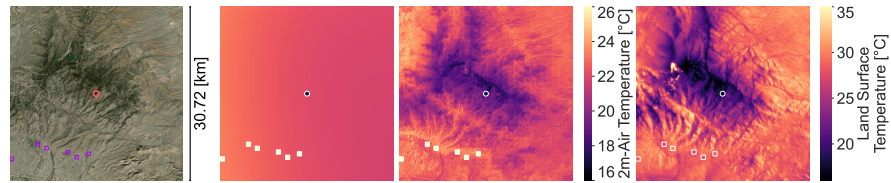
For dewpoint, our micro-weather fields similarly recover dewpoint gradients with topography and vegetation. In mountainous terrain, such as in the Sawtooth Range in Idaho (Figure 3c), lower dewpoint values are inferred at higher elevations and along ridgelines, while higher dewpoint is predicted in valleys. These gradients are absent from the ERA5 field and cannot be recovered through station interpolation alone due to sparse observations, especially in rural areas. In arid regions such as Calexico,

Temperature

a Urban surfaces are hotter than vegetated areas (Washington, D.C.)



b Temperature decreases with elevation (Mount Lemmon, Tucson, Arizona)

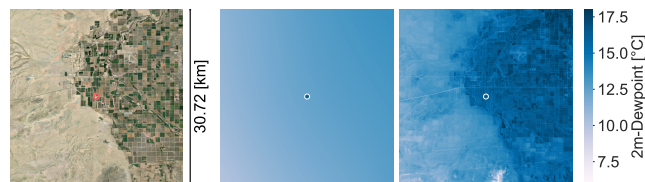


Dewpoint

c Dewpoint decreases with elevation (Bonanza, Sawtooth Range, Idaho)

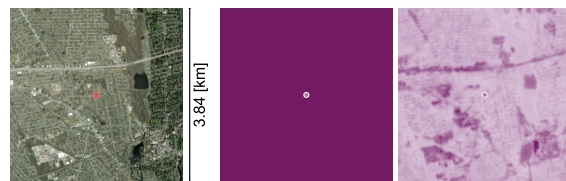


d Crop transpiration increases dewpoint (Calexico, California)

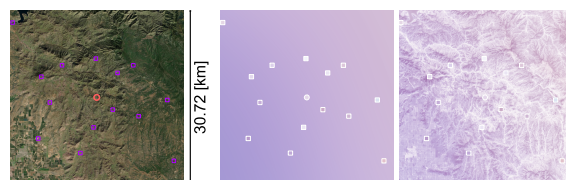


Wind

e Wind speed is higher over open areas and roads (Long Island, New York)



f Higher winds occur over ridges, with wind shadows in the lee (Yokuts Valley, California)



■ Backbone ○ Target



Fig. 3 Physically coherent meter-scale structure in inferred near-surface weather fields. Case studies comparing inferred 10m resolution fields with ERA5 reanalysis. Satellite imagery¹ is shown for spatial context. For temperature panels, land surface temperature from ECOSTRESS is included for qualitative comparison. (a) Urban surfaces are hotter than vegetated areas (Washington, D.C.). (b) Temperature decreases with elevation (Mount Lemmon, Arizona). (c) Dewpoint likewise decreases with elevation (Sawtooth Range, Idaho). (d) Crop transpiration increases humidity (Calexico, California). (e) Wind speed is higher over open areas and roads and lower over built-up and forested areas (Long Island, New York). (f) Higher winds occur over ridges; a southwesterly wind corresponds to windward-leeward contrasts in wind speed (Yokuts Valley, California).

CA (Figure 3d), our micro-weather field captures the contrast between high-humidity irrigated crop fields and low-humidity desert. Meanwhile, ERA5 reflects the average dewpoint in the region, which is dominated by desert conditions, and cannot resolve the fine-scale differences.

Lastly, the inferred near-surface wind fields recover coherent fine-scale structure for both wind speed and direction. In Long Island, NY (Figure 3e), for example, the inferred field shows lower wind speeds over built-up and forested areas and higher speeds over open surfaces. These patterns are consistent with different surface roughness and drag coefficients across land cover types. In mountainous regions, inferred wind speed varies with exposure, with higher wind speeds along ridgelines and lower speeds in sheltered valleys (Figures A5, A6 and A10). In a snapshot from Yokuts Valley, CA (Figure 3f), directional patterns also persist across the region of inference. Under predominantly southeasterly winds inherited from ERA5, the inferred field shows higher speeds on the southeastern sides of ridges and lower speeds on the northwestern sides. Again, neither ERA5 nor station interpolation alone can recover these patterns due to coarseness and sparsity, respectively. These examples illustrate that the large reduction in wind error relative to ERA5 arises from both correction of mean wind magnitude bias and recovery of fine-scale, surface-driven wind structure.

Discussion

Our results demonstrate that a substantial fraction of near-surface micro-scale weather variability is statistically recoverable by combining coarse atmospheric dynamics with sparse in situ observations and high-resolution Earth observation of the land surface. Across the contiguous U.S., the inferred micro-weather fields improve quantitative agreement with held-out weather stations and capture spatially coherent fine-scale structure at tens to hundreds of meters, as evidenced by lower overall errors, increased spatial variance explained, physically-interpretable inferred phenomena, and qualitative agreement with independent space-borne observations.

Conceptually, the statistically recoverable component of micro-weather is distinct from both the large-scale atmospheric forcing present in today’s weather models and small-scale, turbulence-dominated variability. When the large-scale atmospheric state is known, a portion of near-surface variability at tens to hundreds of meters is predictably shaped by static or slowly varying surface characteristics such as land cover, vegetation, urban structure, and topography. By conditioning on these surface features, the inference framework recovers predictable spatial structure at sub-grid resolutions. Our approach complements numerical weather prediction and emerging weather foundation models: whereas those efforts primarily seek to extend forecast horizon or emulate atmospheric dynamics at kilometer-scale grids, we instead target higher spatial resolution. Because it does not explicitly resolve atmospheric

¹All the high resolution image sources used for contextualisation in the document were taken from Tiles © Esri – Source: Esri, i-cubed, USDA, USGS, AEX, GeoEye, Getmapping, Aerogrid, IGN, IGP, UPR-EGP, and the GIS User Community

dynamics at meter-scale, our approach captures a component of micro-weather in a computationally feasible way that can scale to the continent level.

The results also reveal limits to the sub-kilometer meteorology recoverable with this approach. Improvements over ERA5 are strongest in regions of complex terrain, heterogeneous land cover, or strong surface-atmosphere coupling, and weaker in regions such as the northern Great Plains, where surface properties are more homogeneous and near-surface conditions are often dominated by large-scale atmospheric forcing. In other words, there exist regional differences in the amount of fine-scale structure that is absent from reanalysis and therefore available to be recovered. Furthermore, a substantial portion of sub-grid variability — particularly in wind direction and magnitude — remains difficult to capture. For example, complex terrain around the Columbia River Gorge at the border of Oregon and Washington creates changes in wind direction over short distances, but wind directions in our inferred field do not deviate from the main ERA5 direction (Figure A10). Such gaps may arise from errors estimating the coarse atmospheric state, limited spatial context in the Earth observation inputs, sparse station coverage, or fine-scale dynamics that are not represented in the inference framework. In some regions, broader spatial context, denser observations, or additional Earth observation modalities could enable recovery of additional micro-scale structure. However, other components of near-surface variance may require explicit resolution of meter-scale atmospheric dynamics, placing a ceiling on the performance of purely statistical inference approaches.

Validation of micro-weather at fine spatial scales remains challenging and is constrained by observational availability. In this study, we assess micro-weather where observations permit, combining evaluation of error reduced at held-out stations, analysis of spatial variance captured for fixed time stamps, and qualitative comparison with ECOSTRESS land surface temperature observations. Nonetheless, because surface weather stations are absent over open water, the inferred micro-weather fields are not validated for water bodies and should not be interpreted there. Furthermore, many regions contain only a small number of stations per reanalysis grid cell, limiting direct assessment of spatial structure. Future work could leverage denser observational networks, targeted field campaigns, or, in the case of wind, high-resolution large-eddy simulations to validate micro-scale inference.

Improved representation of near-surface temperature, humidity, and wind at meter scales could benefit urban heat exposure assessment, wind power forecasting, wild-fire trajectory prediction, and air pollutant transport modeling. Beyond weather, this framework illustrates how coarse dynamical models and high-resolution Earth observation can be combined to infer fine-scale structure, providing a general template for statistical downscaling across the Earth sciences.

References

- [1] Wang, S., Zhan, W., Zhou, B., Tong, S., Chakraborty, T., Wang, Z., Huang, K., Du, H., Middel, A., Li, J., Liu, Z., Li, L., Huang, F., Li, M.: Dual impact of global urban overheating on mortality. *Nature Climate Change* **15**(5), 497–504 (2025) <https://doi.org/10.1038/s41558-025-02303-3>
- [2] Li, L., Zhan, W., Hu, L., Chakraborty, T., Wang, Z., Fu, P., Wang, D., Liao, W., Huang, F., Fu, H., Li, J., Liu, Z., Du, H., Wang, S.: Divergent urbanization-induced impacts on global surface urban heat island trends since 1980s. *Remote Sensing of Environment* **295**, 113650 (2023) <https://doi.org/10.1016/j.rse.2023.113650>
- [3] Giebel, G., Brownsword, R., Kariniotakis, G., Denhard, M., Draxl, C.: The State-of-the-Art in Short-Term Prediction of Wind Power: A Literature Overview. <https://doi.org/10.11581/DTU:00000017>
- [4] Eghdami, M., Muñoz, P.A.J.y., DeCastro, A.: Sensitivity to the representation of wind for wildfire rate of spread: Case studies with the community fire behavior model. *Fire* **8**(4) (2025) <https://doi.org/10.3390/fire8040135>
- [5] Cruz, M.G., Alexander, M.E.: The 10% wind speed rule of thumb for estimating a wildfire’s forward rate of spread in forests and shrublands. *Annals of Forest Science* **76**(2), 44 (2019)
- [6] Baklanov, A., Grimmond, S., Mahura, A., Athanassiadou, M. (eds.): *Meteorological and Air Quality Models for Urban Areas*, 1st edn. Springer, Berlin, Heidelberg (2009). <https://doi.org/10.1007/978-3-642-00298-4>
- [7] Giorgi, F., Mearns, L.O.: Approaches to the simulation of regional climate change: A review. *Reviews of Geophysics* **29**(2), 191–216 (1991) <https://doi.org/10.1029/90RG02636>
- [8] Rummukainen, M.: State-of-the-art with regional climate models. *WIREs Climate Change* **1**(1), 82–96 (2010) <https://doi.org/10.1002/wcc.8>
- [9] Chandler, R.E.: Multisite, multivariate weather generation based on generalised linear models. *Environmental Modelling & Software* **134**, 104867 (2020) <https://doi.org/10.1016/j.envsoft.2020.104867>
- [10] Schär, C., Fuhrer, O., Arteaga, A., Ban, N., Charpilloz, C., Di Girolamo, S., Hentgen, L., Hoefler, T., Lapillonne, X., Leutwyler, D., Osterried, K., Panosetti, D., Rüdisühli, S., Schlemmer, L., Schulthess, T.C., Sprenger, M., Ubbiali, S., Wernli, H.: Kilometer-Scale Climate Models: Prospects and Challenges. *Bulletin of the American Meteorological Society* **101**(5), 567–587 (2020) <https://doi.org/10.1175/BAMS-D-18-0167.1>

- [11] Jijón, J.D., Gaudry, K.-H., Constante, J., Valencia, C.: Augmenting the spatial resolution of climate-change temperature projections for city planners and local decision makers. *Environmental Research Letters* **16**(5), 054028 (2021) <https://doi.org/10.1088/1748-9326/abf7f2>
- [12] Lam, R., Sanchez-Gonzalez, A., Willson, M., Wirnsberger, P., Fortunato, M., Alet, F., Ravuri, S., Ewalds, T., Eaton-Rosen, Z., Hu, W., Merose, A., Hoyer, S., Holland, G., Vinyals, O., Stott, J., Pritzel, A., Mohamed, S., Battaglia, P.: Learning skillful medium-range global weather forecasting. *Science* **382**(6677), 1416–1421 (2023) <https://doi.org/10.1126/science.adi2336>
- [13] Kurth, T., Subramanian, S., Harrington, P., Pathak, J., Mardani, M., Hall, D., Miele, A., Kashinath, K., Anandkumar, A.: Fourcastnet: Accelerating global high-resolution weather forecasting using adaptive fourier neural operators. In: *Proceedings of the Platform for Advanced Scientific Computing Conference. PASC '23*. Association for Computing Machinery, New York, NY, USA (2023). <https://doi.org/10.1145/3592979.3593412> . <https://doi.org/10.1145/3592979.3593412>
- [14] Nguyen, T., Brandstetter, J., Kapoor, A., Gupta, J.K., Grover, A.: Climax: A foundation model for weather and climate. In: Krause, A., Brunskill, E., Cho, K., Engelhardt, B., Sabato, S., Scarlett, J. (eds.) *Proceedings of the 40th International Conference on Machine Learning. Proceedings of Machine Learning Research*, vol. 202, pp. 25904–25938. PMLR, ??? (2023). <https://proceedings.mlr.press/v202/nguyen23a.html>
- [15] Bi, K., Xie, L., Zhang, H., Chen, X., Gu, X., Tian, Q.: Accurate medium-range global weather forecasting with 3d neural networks. *Nature* **619**(7970), 533–538 (2023)
- [16] Bodnar, C., Bruinsma, W.P., Lucic, A., Stanley, M., Allen, A., Brandstetter, J., Garvan, P., Riechert, M., Weyn, J.A., Dong, H., Gupta, J.K., Thambiratnam, K., Archibald, A.T., Wu, C.-C., Heider, E., Welling, M., Turner, R.E., Perdikaris, P.: A foundation model for the Earth system. *Nature* **641**(8065), 1180–1187 (2025) <https://doi.org/10.1038/s41586-025-09005-y>
- [17] Schmude, J., Roy, S., Trojak, W., Jakubik, J., Civitarese, D.S., Singh, S., Kuehnert, J., Ankur, K., Gupta, A., Phillips, C.E., Kienzler, R., Szwarcman, D., Gaur, V., Shinde, R., Lal, R., Da Silva, A., Diaz, J.L.G., Jones, A., Pfreundschuh, S., Lin, A., Sheshadri, A., Nair, U., Anantharaj, V., Hamann, H., Watson, C., Maskey, M., Lee, T.J., Moreno, J.B., Ramachandran, R.: Prithvi WxC: Foundation Model for Weather and Climate. *arXiv* (2024)
- [18] Price, I., Sanchez-Gonzalez, A., Alet, F., Andersson, T.R., El-Kadi, A., Masters, D., Ewalds, T., Stott, J., Mohamed, S., Battaglia, P., Lam, R., Willson, M.: Probabilistic weather forecasting with machine learning. *Nature* **637**(8044), 84–90 (2025) <https://doi.org/10.1038/s41586-024-08252-9>

- [19] Alet, F., Price, I., El-Kadi, A., Masters, D., Markou, S., Andersson, T.R., Stott, J., Lam, R., Willson, M., Sanchez-Gonzalez, A., Battaglia, P.: Skillful Joint Probabilistic Weather Forecasting from Marginals. arXiv (2025). <https://doi.org/10.48550/arXiv.2506.10772>
- [20] Satoh, M., Stevens, B., Judt, F., Khairoutdinov, M., Lin, S.-J., Putman, W.M., Düben, P.: Global cloud-resolving models. *Current Climate Change Reports* **5**(3), 172–184 (2019) <https://doi.org/10.1007/s40641-019-00131-0>
- [21] Prein, A.F., Rasmussen, R., Stephens, G.: Challenges and advances in convection-permitting climate modeling. *Bulletin of the American Meteorological Society* **98**(5), 1027–1030 (2017) <https://doi.org/10.1175/BAMS-D-16-0263.1>
- [22] Wedi, N.P., Polichtchouk, I., Dueben, P., Anantharaj, V.G., Bauer, P., Boussetta, S., Browne, P., Deconinck, W., Gaudin, W., Hadade, I., Hatfield, S., Iffrig, O., Lopez, P., Maciel, P., Mueller, A., Saarinen, S., Sandu, I., Quintino, T., Vitart, F.: A baseline for global weather and climate simulations at 1 km resolution. *Journal of Advances in Modeling Earth Systems* **12**(11), 2020–002192 (2020) <https://doi.org/10.1029/2020MS002192> <https://agupubs.onlinelibrary.wiley.com/doi/pdf/10.1029/2020MS002192>. e2020MS002192 10.1029/2020MS002192
- [23] European Centre for Medium-Range Weather Forecasts: Ecmwf strategy 2025–2034. Technical report, European Centre for Medium-Range Weather Forecasts (ECMWF), Reading, UK (December 2024). <https://doi.org/10.21957/05dd9b657e> . <https://www.ecmwf.int/en/about/strategy>
- [24] Bryan, G.H., Wyngaard, J.C., Fritsch, J.M.: Resolution requirements for the simulation of deep moist convection. *Monthly Weather Review* **131**(10), 2394–2416 (2003) [https://doi.org/10.1175/1520-0493\(2003\)131<2394:RRFTSO>2.0.CO;2](https://doi.org/10.1175/1520-0493(2003)131<2394:RRFTSO>2.0.CO;2)
- [25] Mirocha, J., Kosović, B., Kirkil, G.: Resolved turbulence characteristics in large-eddy simulations nested within mesoscale simulations using the weather research and forecasting model. *Monthly Weather Review* **142**(2), 806–831 (2014) <https://doi.org/10.1175/MWR-D-13-00064.1>
- [26] Schalkwijk, J., Jonker, H.J.J., Siebesma, A.P., Meijgaard, E.V.: Weather forecasting using gpu-based large-eddy simulations. *Bulletin of the American Meteorological Society* **96**(5), 715–723 (2015) <https://doi.org/10.1175/BAMS-D-14-00114.1>
- [27] Ekström, M., Grose, M.R., Whetton, P.H.: An appraisal of downscaling methods used in climate change research. *WIREs Climate Change* **6**(3), 301–319 (2015) <https://doi.org/10.1002/wcc.339> <https://wires.onlinelibrary.wiley.com/doi/pdf/10.1002/wcc.339>

- [28] Bauer, P., Thorpe, A., Brunet, G.: The quiet revolution of numerical weather prediction. *Nature* **525**(7567), 47–55 (2015) <https://doi.org/10.1038/nature14956>
- [29] Drusch, M., Del Bello, U., Carlier, S., Colin, O., Fernandez, V., Gascon, F., Hoersch, B., Isola, C., Laberinti, P., Martimort, P., Meygret, A., Spoto, F., Sy, O., Marchese, F., Bargellini, P.: Sentinel-2: Esa’s optical high-resolution mission for gmes operational services. *Remote Sensing of Environment* **120**, 25–36 (2012) <https://doi.org/10.1016/j.rse.2011.11.026> . The Sentinel Missions - New Opportunities for Science
- [30] Yang, L., Jin, S., Danielson, P., Homer, C., Gass, L., Bender, S.M., Case, A., Costello, C., Dewitz, J., Fry, J., Funk, M., Granneman, B., Liknes, G.C., Rigge, M., Xian, G.: A new generation of the united states national land cover database: Requirements, research priorities, design, and implementation strategies. *ISPRS Journal of Photogrammetry and Remote Sensing* **146**, 108–123 (2018) <https://doi.org/10.1016/j.isprsjprs.2018.09.006>
- [31] Farr, T.G., Rosen, P.A., Caro, E., Crippen, R., Duren, R., Hensley, S., Kobrick, M., Paller, M., Rodriguez, E., Roth, L., Seal, D., Shaffer, S., Shimada, J., Umland, J., Werner, M., Oskin, M., Burbank, D., Alsdorf, D.: The shuttle radar topography mission. *Reviews of Geophysics* **45**(2) (2007) <https://doi.org/10.1029/2005RG000183> <https://agupubs.onlinelibrary.wiley.com/doi/pdf/10.1029/2005RG000183>
- [32] Fisher, J.B., Lee, B., Purdy, A.J., Halverson, G.H., Dohlen, M.B., Cawse-Nicholson, K., Wang, A., Anderson, R.G., Aragon, B., Arain, M.A., Baldocchi, D.D., Baker, J.M., Barral, H., Bernacchi, C.J., Bernhofer, C., Biraud, S.C., Bohrer, G., Brunsell, N., Cappelaere, B., Castro-Contreras, S., Chun, J., Conrad, B.J., Cremonese, E., Demarty, J., Desai, A.R., De Ligne, A., Foltýnová, L., Goulden, M.L., Griffis, T.J., Grünwald, T., Johnson, M.S., Kang, M., Kelbe, D., Kowalska, N., Lim, J.-H., Maïnassara, I., McCabe, M.F., Missik, J.E.C., Mohanty, B.P., Moore, C.E., Morillas, L., Morrison, R., Munger, J.W., Posse, G., Richardson, A.D., Russell, E.S., Ryu, Y., Sanchez-Azofeifa, A., Schmidt, M., Schwartz, E., Sharp, I., Šigut, L., Tang, Y., Hulley, G., Anderson, M., Hain, C., French, A., Wood, E., Hook, S.: Ecostress: Nasa’s next generation mission to measure evapotranspiration from the international space station. *Water Resources Research* **56**(4), 2019–026058 (2020) <https://doi.org/10.1029/2019WR026058> <https://agupubs.onlinelibrary.wiley.com/doi/pdf/10.1029/2019WR026058>. e2019WR026058 2019WR026058
- [33] Brown, C.F., Kazmierski, M.R., Pasquarella, V.J., Rucklidge, W.J., Samsikova, M., Zhang, C., Shelhamer, E., Lahera, E., Wiles, O., Ilyushchenko, S., Gorelick, N., Zhang, L.L., Alj, S., Schechter, E., Askay, S., Guinan, O., Moore, R., Boukouvalas, A., Kohli, P.: AlphaEarth Foundations: An Embedding Field Model for Accurate and Efficient Global Mapping from Sparse Label Data. *arXiv* (2025). <https://doi.org/10.48550/arXiv.2507.22291>

- [34] Vaswani, A., Shazeer, N., Parmar, N., Uszkoreit, J., Jones, L., Gomez, A.N., Kaiser, L., Polosukhin, I.: Attention is All you Need. In: *Advances in Neural Information Processing Systems*, vol. 30. Long Beach, CA, USA (2017)
- [35] Good, E.J.: An in situ-based analysis of the relationship between land surface “skin” and screen-level air temperatures. *Journal of Geophysical Research: Atmospheres* **121**(15), 8801–8819 (2016) <https://doi.org/10.1002/2016JD025318> <https://agupubs.onlinelibrary.wiley.com/doi/pdf/10.1002/2016JD025318>
- [36] Hersbach, H., Bell, B., Berrisford, P., Hirahara, S., Horányi, A., Muñoz-Sabater, J., Nicolas, J., Peubey, C., Radu, R., Schepers, D., Simmons, A., Soci, C., Abdalla, S., Abellan, X., Balsamo, G., Bechtold, P., Biavati, G., Bidlot, J., Bonavita, M., De Chiara, G., Dahlgren, P., Dee, D., Diamantakis, M., Dragani, R., Flemming, J., Forbes, R., Fuentes, M., Geer, A., Haimberger, L., Healy, S., Hogan, R.J., Hólm, E., Janisková, M., Keeley, S., Laloyaux, P., Lopez, P., Lupu, C., Radnoti, G., de Rosnay, P., Rozum, I., Vamborg, F., Villaume, S., Thépaut, J.-N.: The ERA5 global reanalysis. *Quarterly Journal of the Royal Meteorological Society* **146**(730), 1999–2049 (2020) <https://doi.org/10.1002/qj.3803>
- [37] Takaku, J., Tadono, T., Tsutsui, K.: Generation of High Resolution Global DSM from ALOS PRISM. *The International Archives of the Photogrammetry, Remote Sensing and Spatial Information Sciences* **XL-4**, 243–248 (2014) <https://doi.org/10.5194/isprsarchives-XL-4-243-2014>
- [38] European Space Agency: Copernicus Global Digital Elevation Model (2024). <https://doi.org/10.5069/G9028PQB>
- [39] Zanaga, D., Van De Kerchove, R., Daems, D., De Keersmaecker, W., Brockmann, C., Kirches, G., Wevers, J., Cartus, O., Santoro, M., Fritz, S., et al.: ESA WorldCover 10 m 2021 v200 (2022)
- [40] Pasquarella, V.J., Brown, C.F., Czerwinski, W., Rucklidge, W.J.: Comprehensive quality assessment of optical satellite imagery using weakly supervised video learning. In: *2023 IEEE/CVF Conference on Computer Vision and Pattern Recognition Workshops (CVPRW)*, pp. 2125–2135. IEEE, Vancouver, BC, Canada (2023). <https://doi.org/10.1109/CVPRW59228.2023.00206>
- [41] Hook, S., Hulley, G.: ECOSTRESS Swath Land Surface Temperature and Emissivity Instantaneous L2 Global 70 m V002. NASA EOSDIS Land Processes Distributed Active Archive Center (DAAC) data set (2022)
- [42] Jin, M., Dickinson, R.E.: Land surface skin temperature climatology: Benefitting from the strengths of satellite observations. *Environmental Research Letters* **5**(4), 044004 (2010) <https://doi.org/10.1088/1748-9326/5/4/044004>
- [43] Good, E.J., Ghent, D.J., Bulgin, C.E., Remedios, J.J.: A spatiotemporal analysis of the relationship between near-surface air temperature and satellite land surface

- temperatures using 17 years of data from the ATSR series. *Journal of Geophysical Research: Atmospheres* **122**(17), 9185–9210 (2017) <https://doi.org/10.1002/2017JD026880>
- [44] Mo, Y., Pepin, N., Lovell, H.: Understanding temperature variations in mountainous regions: The relationship between satellite-derived land surface temperature and in situ near-surface air temperature. *Remote Sensing of Environment* **318**, 114574 (2025) <https://doi.org/10.1016/j.rse.2024.114574>
- [45] Zhang, H., Mahmood, A.N., Hu, T., Mallick, K., Didry, Y., Hitzelberger, P., Szantoi, Z., Pérez-Planells, L., Göttsche, F.M., Hulley, G.C., Hook, S.J.: Global evaluation of high-resolution ECOSTRESS land surface temperature and emissivity products: Collection 1 versus Collection 2. *Remote Sensing of Environment* **326**, 114799 (2025) <https://doi.org/10.1016/j.rse.2025.114799>
- [46] Dong, B., Song, R., Luo, L., Jiang, X., Chen, H., Li, B., Wang, Y.: Quantitative Evaluation of Complex Terrain Effects on Land Surface Temperature: A Data-driven Coupling Model of Dynamic and Static Features (2025). <https://doi.org/10.2139/ssrn.5384696>
- [47] Yang, Q., Giezendanner, J., Civitarese, D.S., Jakubik, J., Schmitt, E., Chandra, A., Vila, J., Hohl, D., Hill, C., Watson, C., Wang, S.: Local Off-Grid Weather Forecasting With Multi-Modal Earth Observation Data. *Journal of Advances in Modeling Earth Systems* **17**(12), 2025–005207 (2025) <https://doi.org/10.1029/2025MS005207>
- [48] Cong, Y., Khanna, S., Meng, C., Liu, P., Rozi, E., He, Y., Burke, M., Lobell, D.B., Ermon, S.: SatMAE: Pre-training transformers for temporal and multi-spectral satellite imagery. In: Oh, A.H., Agarwal, A., Belgrave, D., Cho, K. (eds.) *Advances in Neural Information Processing Systems* (2022). <https://openreview.net/forum?id=WBhqzPF6KYH>
- [49] Reed, C.J., Gupta, R., Li, S., Brockman, S., Funk, C., Clipp, B., Keutzer, K., Candido, S., Uyttendaele, M., Darrell, T.: Scale-mae: A scale-aware masked autoencoder for multiscale geospatial representation learning. In: *Proceedings of the IEEE/CVF International Conference on Computer Vision (ICCV)*, pp. 4088–4099 (2023)
- [50] Klemmer, K., Rolf, E., Robinson, C., Mackey, L., Rußwurm, M.: Sat-clip: global, general-purpose location embeddings with satellite imagery. *AAAI'25/IAAI'25/EAAI'25*. AAAI Press, ??? (2025). <https://doi.org/10.1609/aaai.v39i4.32457> . <https://doi.org/10.1609/aaai.v39i4.32457>
- [51] Astruc, G., Gonthier, N., Mallet, C., Landrieu, L.: Anysat: One earth observation model for many resolutions, scales, and modalities. In: *Proceedings of the IEEE/CVF Conference on Computer Vision and Pattern Recognition (CVPR)*, pp. 19530–19540 (2025)

- [52] Waldmann, L., Shah, A., Wang, Y., Lehmann, N., Stewart, A., Xiong, Z., Zhu, X.X., Bauer, S., Chuang, J.: Panopticon: Advancing any-sensor foundation models for earth observation. In: Proceedings of the IEEE/CVF Conference on Computer Vision and Pattern Recognition (CVPR) Workshops, pp. 2229–2239 (2025)
- [53] Dosovitskiy, A., Beyer, L., Kolesnikov, A., Weissenborn, D., Zhai, X., Unterthiner, T., Dehghani, M., Minderer, M., Heigold, G., Gelly, S., Uszkoreit, J., Houlsby, N.: An Image is Worth 16x16 Words: Transformers for Image Recognition at Scale. In: 9th International Conference on Learning Representations, ICLR 2021, Virtual Event, Austria, May 3-7, 2021. OpenReview.net, ??? (2021)
- [54] Lin, H., Cheng, X., Wu, X., Shen, D.: CAT: Cross Attention in Vision Transformer. In: 2022 IEEE International Conference on Multimedia and Expo (ICME), pp. 1–6. IEEE, Taipei, Taiwan (2022). <https://doi.org/10.1109/ICME52920.2022.9859720>
- [55] Chen, C.-F.R., Fan, Q., Panda, R.: CrossViT: Cross-Attention Multi-Scale Vision Transformer for Image Classification. In: 2021 IEEE/CVF International Conference on Computer Vision (ICCV), pp. 347–356. IEEE, Montreal, QC, Canada (2021). <https://doi.org/10.1109/ICCV48922.2021.00041>
- [56] Rußwurm, M., Klemmer, K., Rolf, E., Zbinden, R., Tuia, D.: Geographic Location Encoding with Spherical Harmonics and Sinusoidal Representation Networks. In: The Twelfth International Conference on Learning Representations, ICLR 2024, Vienna, Austria, May 7-11, 2024. OpenReview.net, ??? (2024)
- [57] Wu, H., Xiao, B., Codella, N., Liu, M., Dai, X., Yuan, L., Zhang, L.: CvT: Introducing Convolutions to Vision Transformers. In: 2021 IEEE/CVF International Conference on Computer Vision (ICCV), pp. 22–31. IEEE, Montreal, QC, Canada (2021). <https://doi.org/10.1109/ICCV48922.2021.00009>
- [58] Kingma, D.P., Ba, J.: Adam: A Method for Stochastic Optimization. arXiv (2017). <https://doi.org/10.48550/arXiv.1412.6980>
- [59] Delaunay, B.N.: Sur la sphère vide. A la mémoire de Georges Voronoï. Известия Российской академии наук. Серия математическая **6**, 793–800 (1934)

Methods

Data

Point-based Weather Observations

The Meteorological Assimilation Data Ingest System (MADIS²) is a database provided by the National Oceanic and Atmospheric Administration (NOAA) that contains meteorological observations from stations worldwide. MADIS collects data from both NOAA and non-NOAA sources, encompassing observation networks from US federal, state, and transportation agencies, universities, volunteer networks, and private sectors such as airlines, as well as public-private partnerships like the Citizen Weather Observer Program. We here use the MADIS LDAD Mesonet source. From MADIS, we selected four variables: 2 m temperature, 2 m dewpoint temperature, 10 m wind speed and 10 m wind direction. From wind speed and direction, we derive the u and v components of wind, i.e., the portions of the wind that blow west to east and south to north, respectively.

In this work, we focus on stations over the contiguous United States (CONUS). We only keep averaged hourly observations with the quality flag “Screened” or “Verified”. We processed four years of hourly averaged data from 2020 to 2023. Furthermore, we then only keep stations with at least 60% of data of sufficient quality over the five years, leaving us with 11,849 stations (Figure 5). For training, missing values are interpolated, but all results are reported on true observed values only. Each station thus has a maximum of 35,040 hourly observations.

Kilometer-scale Weather Reanalysis

The ECMWF Reanalysis v5 (ERA5) dataset [36] from the European Centre for Medium-Range Weather Forecasts (ECMWF) is a comprehensive gridded reanalysis product that integrates model data with global observations. ERA5 provides global hourly data at a $0.25^\circ \times 0.25^\circ$ resolution, equivalent to 31 km/pixel at the equator, covering the period from 1950 to present. It includes weather data both at the surface and at different pressure levels. For this work, we curated 4 years (2020 to 2023) of surface variables over CONUS: 10 m wind u , 10 m wind v , 2 m temperature, and 2 m dewpoint temperature. Using bilinear interpolation, ERA5 is interpolated to each backbone station and target location.

Meter-scale Satellite Imagery

In our main model specification, we use embeddings from the AlphaEarth geospatial foundation model [33] to provide information about land cover, terrain, and other surface characteristics to the micro-weather model. We also experimented with learning features end-to-end from raw Sentinel-2 imagery, DEM, DSM, and a land cover map. Below we describe the data used in both approaches.

²<https://madis.ncep.noaa.gov/>

The AlphaEarth foundation model ingests a diverse set of remote sensing modalities and delivers, through Google Earth Engine, a 64-dimensional embedding vector that summarizes all modalities at a given location on Earth. Datasets used to train the AlphaEarth model include optical satellite data (Sentinel-2, Landsat 8/9), radar satellite data (Sentinel-1, ALOS PALSAR-2), LiDAR satellite data (GEDI), land cover, DEM, natural language descriptions (geolocated Wikipedia articles, GBIF), and environmental and climate data (GRACE and monthly ERA5-Land). AlphaEarth then summarizes this wide range of modalities with a Space Time Precision (STP) Encoder [33]. Embeddings from AlphaEarth are delivered at 10 m resolution, corresponding to the highest-resolution datasets ingested by the model (Sentinel-1 and Sentinel-2).

Separately, we also prepare raw and derived satellite image chips for each weather station location to test end-to-end feature learning (Figure 4). These image chips are static in time and consist of 30 m-resolution DSM, and DEM and 10 m-resolution land cover and Sentinel-2 imagery. We construct 16×16 pixel 30 m-resolution chips and 48×48 pixel 10 m-resolution chips centered on each weather station. Each chip thus covers 480×480 meters around each station. The DSM data are from the JAXA ALOS DSM: Global 30m v3.2 [37], and the DEM data are from Copernicus DEM GLO-30: Global 30m Digital Elevation Model [38]. From the DEM, we further derive the slope and aspect at each pixel, with aspect separated into northness and eastness to obtain two cyclic variables within the range -1 to 1 . We use ESA WorldCover 10 m v200 for land cover data [39] and retain 7 categories: Tree Cover, Grassland/Herbaceous wetland, Shrubland, Cropland, Bare/Sparse Vegetation, Built-up and Permanent Water Bodies. For every location, we also create four seasonal Sentinel-2 composites, each comprised of the four 10 m resolution bands: Blue, Green, Red, and NIR. For each season, we select all the images that fall within the given time period, mask out clouds [40], and finally compute the median value for each pixel. We define winter as December 21 to March 20, spring as March 21 to June 21, summer as June 22 to September 22, and fall as September 23 to December 20. We use imagery from one year (December 2023 to December 2024) for simplicity.

ECOSTRESS Land Surface Temperature (LST)

ECOSTRESS is an instrument aboard the International Space Station that senses land surface temperature and emissivity (LST&E) at 70 m resolution with 4 day revisit [41]. As LST and air temperature are correlated [35], we use the LST data product to qualitatively assess the micro-weather model’s ability to infer sub-grid temperature variations.

However, the 2 m air temperature inferred in this work differs from ECOSTRESS LST in several important ways, and their comparison requires careful interpretation. First, our air temperature is averaged hourly, while ECOSTRESS-sensed LST is instantaneous. Second, the relationship between ground temperature and 2 m air temperature is highly non-linear [42–45]. A diurnal cycle exists: at night, LST and air temperature are more closely correlated, whereas during the day, the differences can become substantial [43]. Over vegetated areas, LST is generally lower than air temperature during the day due to evapotranspiration [43]. Bare and sparsely vegetated

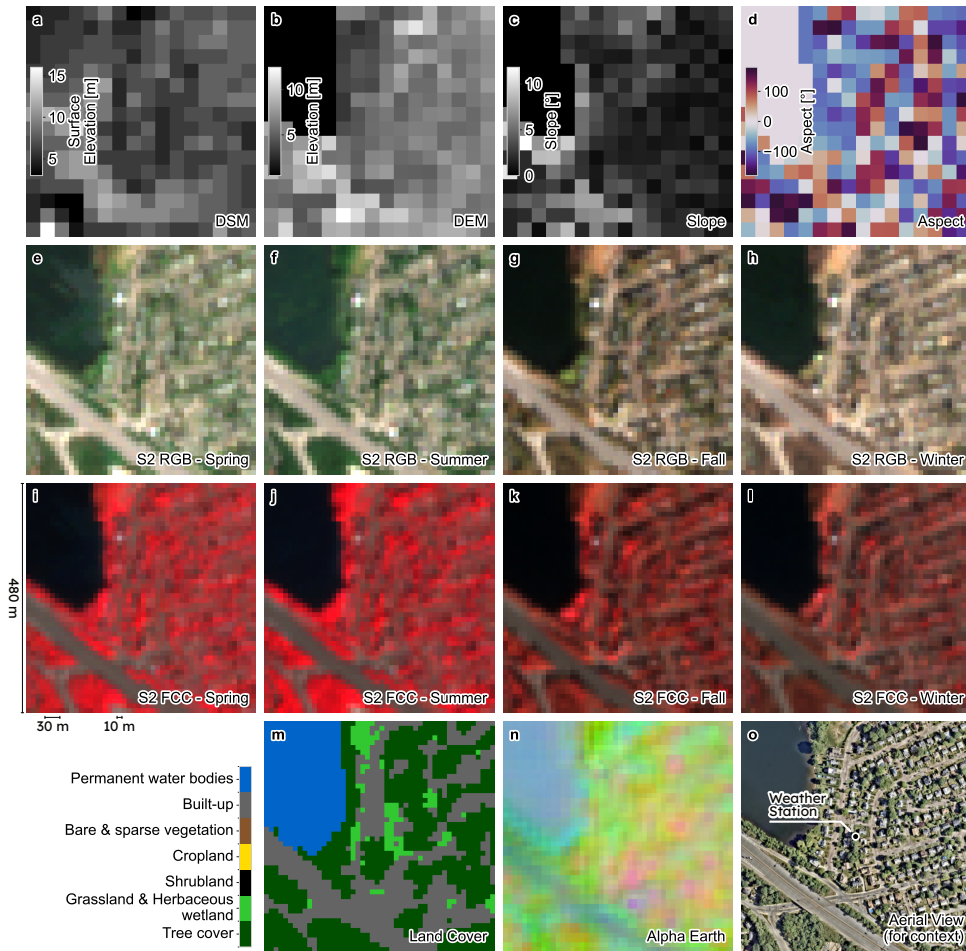


Fig. 4 Example of Earth observation inputs for a given location. Panels (a)–(m) include satellite layers used for the end-to-end learned satellite embedding. (a–d) DSM, DEM, and derived indices. (e–h) Sentinel-2 for spring, summer, fall, and winter seasons visualized in RGB. (i–l) Sentinel-2 for the four seasons visualized as a False Color Composite (FCC; NIR, R, G). (m) Land cover map with seven classes selected (of which only four are present at this location). (n) Geospatial foundation model embeddings produced by AlphaEarth [33]. (o) Aerial image of the same location, not used in the model, for context only.

areas, such as urban regions, exhibit the largest differences between LST and air temperature. Third, satellite-based LST retrievals have higher errors over complex terrain than flat terrain [46]. Beyond measurement errors, the coupling between LST and air temperature weakens with elevation.

For these reasons, we limit comparison of our air temperature fields with ECOSTRESS LST to a qualitative assessment within case studies to establish general spatial correlations and physical plausibility.

Model Architecture

Transformers [34] are a class of neural network architecture that has yielded state-of-the-art results on a variety of applications, including in weather forecasting [12–17, 47] and feature extraction from satellite imagery [33, 48–52]. We model our architecture on a vision transformer (ViT) [53] to capture the spatial relationships between weather reanalysis, weather stations, and satellite embeddings.

In our formulation, data at each location — including weather station locations and arbitrary locations at inference — become a token in the transformer. First, tokenized backbone weather stations are passed through a multi-head residual self-attention mechanism (3 heads, 5 layers per head). In self-attention, the keys (K), queries (Q) values (V) matrices are calculated by multiplying the backbone tokens by three learned weight matrices. The attention mechanism then combines these three matrices to extract the relevant connections between tokens:

$$\text{Attention}(Q, K, V) = \text{softmax} \left(\underbrace{\frac{Q \cdot K^T}{\sqrt{d_k}}}_{\text{Attention Matrix}} \right) V, \quad (1)$$

where d_k is the dimension of the latent space. The output of this self-attention provides the context for the target location in the next step.

Next, cross-attention [34, 54, 55] multiplies the context tokens from self-attention by weight matrices to generate new key (K_c) and value (V_c) matrices. Separately, queries (Q_a) are generated by multiplying the target location tokens by another weight matrix. Cross-attention then becomes a mechanism to extract the relevant information from the interaction of context tokens (from the backbone stations) and target location query:

$$\text{Attention}(Q_a, K_c, V_c) = \text{softmax} \left(\frac{Q_a \cdot K_c^T}{\sqrt{d_k}} \right) V_c. \quad (2)$$

This mechanism allows the model to focus on relevant information from the backbone stations to infer the weather at arbitrary locations. This module is also a multi-head residual transformer with 3 heads and 5 layers per head [34].

Tokenization of Weather Data

At each weather station and target location, the weather station observations and the coarse reanalysis data are tokenized separately, but for both modalities the process is the same. Each variable (temperature, dewpoint, and wind) is first passed through a multi-layer perceptron (MLP) with ReLU activation; then the three variables’ embeddings are concatenated and passed through a final linear layer to produce a single latent vector. For the backbone weather stations, the station and ERA5 modalities are then further concatenated together, whereas for target locations, the ERA5 token becomes the sole starting information for prediction.

Location Encoding

To provide the model with the geolocation of each backbone station and target location, we employed a Global Geographic Location Encoding [56], which encodes the latitude and longitude coordinates of each weather station and target location with spherical harmonics and sinusoidal representation networks. This helps the model build a spatial understanding of the backbone weather stations as well as the relationship in space between backbone stations and the target locations. The location encoding is appended to the weather data tokens.

Satellite Embedding

The model is tasked with extracting from satellite imagery the surface characteristics at each location that are relevant for micro-weather. We compared learning relevant satellite features in an end-to-end fashion and making use of an already-trained geospatial foundation model embedding (AlphaEarth embeddings). In the former, we first harmonized the 10 m and 30 m-resolution data sources with a learned downsampling scheme. We then employed an architecture inspired by CvT [57] to generate tokens from images through the use of convolution neural networks (CNN). We adapted this approach to our satellite data by first applying a depth-wise convolution to each band separately, followed by a point-wise convolution to combine the information from all bands. We then passed the output of this initial embedding through an MLP to map the compressed images to the latent space, and combine it with a skip connection that emphasizes the conditions at weather station location itself.

In the second approach, we simply obtained AlphaEarth embeddings through the Google Earth Engine platform at each station and target location. In both approaches, the satellite embedding was appended to the weather station and ERA5 tokens to characterize each location.

The end-to-end learning and AlphaEarth foundation model approaches performed very similarly, but the latter was slightly better and more lightweight for inference. We therefore show results in the main text for the AlphaEarth specification.

Model Training and Inference

We divided the 11,849 weather stations into 4 groups (Figure 5): backbone, training, validation, and test sets. We placed stations with over 80% of observations flagged as high-quality by the MADIS network into the backbone set (8,180 stations, corresponding to 263,671,049 valid station-time step observations), so that they can supply information on local weather to nearby target locations for as many time steps as possible. Stations whose observations are flagged as high-quality 70–80% of the time were placed in the training set (2,260 stations, 59,888,622 valid observations). Finally, we randomly split the stations with 60–70% high-quality observations into the validation (854 stations, 19,492,371 valid observations) and test sets (555 stations, 12,711,249 valid observations). Stations with fewer than 60% high-quality observations were not used in this study.

The model weights were trained by tasking the model with predicting temperature, dewpoint, and the u, v components of wind at training set stations for hourly time

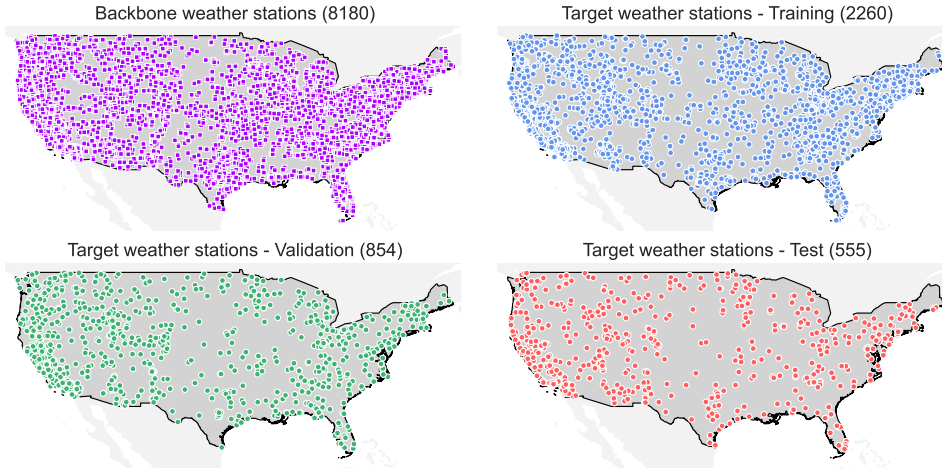


Fig. 5 Spatial partitioning of contiguous U.S. weather stations for training and evaluation. Surface weather stations from NOAA MADIS across the contiguous U.S. are split into four disjoint sets: backbone, training, validation, and test. Only test set stations are used for evaluation.

steps between 2020 and 2023. Models were trained with the Adam optimizer [58] with a learning rate of 10^{-3} modified over epochs with cosine annealing and a weight decay of 10^{-4} . The model checkpoint used for test set evaluation and inference was selected based on the best validation set performance.

At inference time, we downloaded static satellite data or AlphaEarth embeddings at arbitrary target locations. Our micro-weather model then inferred the three near-surface weather variables simultaneously at target locations at any desired time stamp by combining the ERA5 data, backbone weather station data, and satellite embedding at the time stamp of interest. Continuous micro-weather fields at 10 m resolution were generated by tiling the target region (for the AlphaEarth specification, we used 1024×1024 pixel blocks, corresponding to $10.24 \text{ km} \times 10.24 \text{ km}$), which were processed in parallel using cross-attention. Inference was conducted on CPU (36 cores, 250 GB RAM), with the maximum region size primarily constrained by available memory.

Baseline Models

We compared our micro-weather model performance to two baselines: interpolation of backbone weather station data and interpolation of ERA5. To interpolate weather stations, we used a radial basis function with a linear kernel to interpolate temperature, dewpoint, and the u, v components of wind between the backbone station locations to every test station location. For ERA5, we used bilinear interpolation between the ERA5 grid to obtain weather values at test station locations.

Evaluation Metrics

Model performance is evaluated using mean absolute error (MAE), root mean square error (RMSE), vector error, and a spatial coefficient of determination (spatial R^2 ,

or spatial variance explained). Temperature and dewpoint errors are evaluated using scalar metrics (MAE and RMSE; we show MAE in the main text and RMSE in additional tables). Wind errors are evaluated using a vector error metric that jointly accounts for discrepancies in wind speed and direction, as well as scalar metrics for speed and direction separately.

Let i index test stations and t index time steps. All scalar error metrics are computed over individual station-time pairs in the held-out test set, with equal weighting across observations. MAE and RMSE are defined as

$$\text{MAE} = \frac{1}{NT} \sum_{i=1}^N \sum_{t=1}^T |y_{i,t} - m_{i,t}|, \quad \text{RMSE} = \sqrt{\frac{1}{NT} \sum_{i=1}^N \sum_{t=1}^T (y_{i,t} - m_{i,t})^2},$$

where $y_{i,t}$ and $m_{i,t}$ denote station observations and model predictions, respectively. Wind vector error is computed as the Euclidean norm of the difference between predicted and observed horizontal wind vectors u and v , averaged across all station-time observations:

$$\text{Vector error} = \frac{1}{NT} \sum_{i=1}^N \sum_{t=1}^T \sqrt{(u_{i,t} - m_{i,t}^u)^2 + (v_{i,t} - m_{i,t}^v)^2}.$$

Spatial R^2 (spatial variance explained) is computed to quantify how well the model captures spatial structure at a particular snapshot in time. At each time step t , we remove the across-station mean from both observations and predictions so that

$$\tilde{y}_{i,t} = y_{i,t} - \bar{y}_t, \quad \tilde{m}_{i,t} = m_{i,t} - \bar{m}_t,$$

where \bar{y}_t, \bar{m}_t denote spatial means across stations at time t . Spatial R^2 is then defined as

$$R_{\text{spatial}}^2(t) = 1 - \frac{\sum_i (\tilde{y}_{i,t} - \tilde{m}_{i,t})^2}{\sum_i \tilde{y}_{i,t}^2}.$$

For wind, the multivariate R_{spatial}^2 is calculated from the predicted and observed wind vectors:

$$R_{\text{spatial, wind}}^2(t) = 1 - \frac{\sum_i \|\tilde{\mathbf{y}}_{i,t} - \tilde{\mathbf{m}}_{i,t}\|^2}{\sum_i \|\tilde{\mathbf{y}}_{i,t}\|^2},$$

where $\mathbf{y}_{i,t} = (u_{i,t}, v_{i,t})$ and $\mathbf{m}_{i,t} = (m_{i,t}^u, m_{i,t}^v)$.

When reporting a single spatial R^2 metric for a model, we average $R_{\text{spatial}}^2(t)$ across all test time steps.

Satellite Ablation Studies

We conducted four satellite-related ablation experiments: (1) removal of the satellite modality entirely; (2) removal of Sentinel-2 imagery; (3) removal of spatial context in satellite imagery; and (4) comparison of pre-trained AlphaEarth embeddings with end-to-end learned embeddings. In all cases, model architecture, training data, optimization, and evaluation procedures were held fixed.

As discussed in the main text, we sought to understand the importance of local satellite data as a modality on micro-weather inference. In experiment (1), we compared the full model trained with all three modalities — ERA5, backbone weather stations, and local satellite context — to a model trained on only ERA5 and backbone weather station data to determine the contribution of local satellite data. In experiment (2), we compared the complete model to a model with no Sentinel-2 data; i.e., the model is only provided with DSM, DEM, and land cover type information. In experiment (3), we investigated the importance of spatial context in satellite imagery for micro-weather inference. We compared the full model to only keeping the center satellite pixel values, i.e., removing the spatial context around each location. Lastly, in experiment (4), we compared the performance of a model that learned satellite embeddings for micro-weather inference end-to-end versus a model that used pre-computed satellite embeddings from the AlphaEarth geospatial foundation model.

Sensitivity to Backbone Station Proximity and Connectivity

We sought to understand how backbone station distance to a target location and the connectivity of the backbone station network impact micro-weather inference at the target location.

We hypothesized that having backbone weather stations closer to a target location would improve micro-weather inference, since the model would be able to access near-surface weather conditions that are more similar to that target location. To examine this, we computed the distance from test set stations to their nearest $k = 1, 5, 10,$ and 20 backbone stations and plotted station-level error against distance to the nearest k stations.

We also experimented with different connectivities in the weather station network. The network has two components: the backbone weather stations, which are used in self-attention, and the backbone to target location connections, which are used in cross-attention. In the main model specification, both components are fully connected. To assess whether this full connectivity is necessary, we impose sparsity on the attention mechanism by masking attention weights corresponding to disallowed station-station or station-target pairs, while leaving all other aspects of the model unchanged. We perform two experiments, replacing the full connectivity with (i) Delaunay triangulation [59], a method that removes redundant edges and avoids acute angles between edges, or (ii) limiting backbone-to-arbitrary edges to the 20 nearest backbone stations.

Data Availability

ERA5 data are available from ECMWF at <https://cds.climate.copernicus.eu/datasets/reanalysis-era5-single-levels?tab=download>. MADIS data are available from NOAA at <https://madis.ncep.noaa.gov/>. Satellite data were obtained via Google Earth Engine: https://developers.google.com/earth-engine/datasets/catalog/ESA_WorldCover_v200 (Land Cover), https://developers.google.com/earth-engine/datasets/catalog/COPERNICUS_DEM_GLO30 (DEM), https://developers.google.com/earth-engine/datasets/catalog/JAXA_ALOS_AW3D30_V3_2 (DSM), <https://developers.google.com/earth-engine/datasets/catalog/sentinel-2> (Sentinel-2), https://developers.google.com/earth-engine/datasets/catalog/GOOGLE_SATELLITE_EMBEDDING_V1_ANNUAL (AlphaEarth embeddings). The processed dataset will be made public upon acceptance.

Code Availability

Code will be made available to editors and referees upon request, and it will be made publicly available upon publication.

Author Contributions

Conceptualization: J.G., Q.Y., S.W. Data curation: J.G., Q.Y. Formal analysis: J.G., S.W. Funding acquisition: S.W. Investigation: J.G. Methodology: J.G., Q.Y., D.S.C., J.J., E.S., A.C., S.W. Software: J.G. Supervision: S.W. Visualization: J.G., S.W. Writing — original draft: J.G., S.W. Writing — review and editing: All authors.

Competing Interests

E.S., A.C., J.V., and D.H. are employees of Shell Information Technology International Inc. D.S.C, J.J., and C.W. are employees of IBM. The authors declare no other competing interests.

Materials & Correspondence

Correspondence and requests for materials should be addressed to J.G. or S.W.

Extended Data

Temporal Behavior at Held-out Stations

To complement the spatial analyses in the main text, we examine the temporal behavior of inferred micro-weather at held-out test stations. We compare time series of near-surface temperature, dewpoint, and wind against observations, ERA5 interpolation, and station-interpolation baselines at a few representative stations (Figure A1). Across locations and weather variables, the predicted time series follow increases and decreases in large-scale atmospheric dynamics from ERA5 while making adjustments based on backbone weather station measurements and satellite-based surface information. However, the model does not appear to be able to reproduce the high-frequency station-level variability that is not already present in ERA5.

For temperature, the inferred time series generally follow the large-scale temporal evolution imposed by ERA5 while exhibiting persistent offsets that vary across locations and time periods. In regions with strong topographic or land-surface influences, such as Mount Lemmon (Figures A1a and A5), Washington, D.C. (Figure A4), and Bonanza, Idaho (Figure A6), these offsets are consistent over multi-day windows and move predictions closer to station observations.

Dewpoint, similar to air temperature, generally follows large-scale ERA5 temporal patterns. In regions with strong localized humidity, our micro-weather inference can differ from ERA5 to capture patterns similar to those observed at held-out weather stations. An example can be seen in irrigated agriculture in arid regions, such as in the southwestern U.S. (Figure A1b and A7), where dewpoint is markedly higher in irrigated fields than the surrounding area. Here ERA5 reflects the average dewpoint in the region, which is dominated by the aridity of the desert, whereas the micro-weather model reproduces higher dewpoint values over irrigated fields. However, since our satellite data is static, the micro-weather inference cannot capture high-frequency variability over irrigated fields (e.g., high humidity late in the day on July 4, 2023 in Figure A7).

Lastly, time series visualizations reveal that our micro-weather model frequently improves upon ERA5 near-surface wind by reducing the systematically high bias in wind speed, particularly at sheltered stations. In multiple examples (Figure A1c, Figures A4 to A6), the micro-weather model reduces ERA5’s bias by incorporating information from nearby backbone stations and surface characteristics, yielding wind magnitudes that are more consistent with observations while preserving broad temporal variability. At the same time, considerable residual variability in wind speed and direction remains unexplained by the micro-weather model, especially in complex terrain (Figures A5 to A7 and A9), demonstrating limits to recoverable wind structure in our approach.

Satellite Ablation Results

When comparing the full model to a variant trained without satellite inputs, we find that the full model achieves better micro-weather inference as measured by both MAE and spatial variance captured, across all three near-surface weather variables (Figure 2;

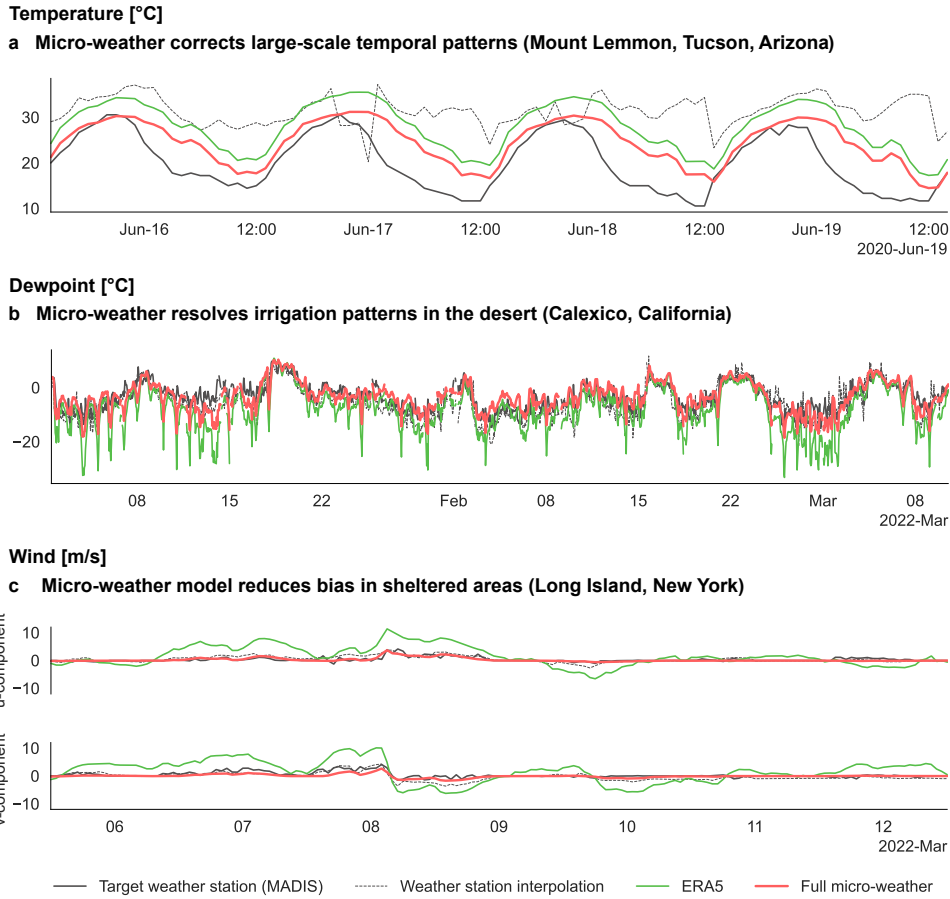


Fig. A1 Temporal behavior of inferred micro-weather at example held-out stations. Hourly time series compare inferred micro-weather fields, ERA5 reanalysis, and weather station interpolation against station observations. **(a)** Station located near mountain summit (Mount Lemmon, Arizona). **(b)** Station located in irrigated crop fields surrounded by desert (Calexico, California). **(c)** Station located in sheltered suburban area (Long Island, New York).

Tables A1 and A2). Relative to the ERA5-interpolation baseline, more than half of the MAE reduction for temperature and dewpoint can be attributed to the addition of the satellite modality, whereas for wind 6% out of the 29% reduction in the vector error occurs after adding satellite data (i.e., combining only ERA5 and backbone weather station data in a deep learning framework reduced wind error by 23%). In the spatial variance metric (spatial R^2), ERA5 interpolation already explains a high proportion of the spatial variance in temperature and dewpoint, with 84% and 87% of variance explained, respectively, across the U.S. on average across all time stamps. Adding backbone weather stations increases the variance captured to 85% and 88%, and adding satellite data further increases variance captured slightly to 86% and 89%.

For wind, ERA5 alone achieves an R^2 of -2% against weather station observations, likely due to its significant bias for near-surface wind. A model that combines backbone stations and ERA5 data can increase the variance explained to 29% . Finally, adding the satellite modality further increases the variance explained to 38% . Together, these results indicate that including satellite-derived surface information improves micro-weather inference relative to models that rely only on ERA5 and backbone weather stations.

Table A1 Spatial R^2 . Spatial variance explained is calculated for each time step over all test stations and then averaged over all time steps.

Model	Temperature	Dewpoint	Wind
Weather station interpolation	0.59	0.74	-0.56
ERA5	0.84	0.87	-0.02
Micro-weather (stations & ERA5)	0.85	0.88	0.29
Full micro-weather (+ Earth observation)	0.86	0.89	0.38

We find that the performance of a micro-weather model trained to learn satellite embeddings end-to-end was slightly worse (about 1% larger temperature/dewpoint MAE and wind vector errors) than a micro-weather model that uses AlphaEarth embeddings to encode static surface features (Table A2). The difference in performance was slightly larger for wind than for temperature and dewpoint, which may reflect the inclusion of additional remote sensing modalities (e.g., radar and lidar) in the AlphaEarth embeddings.

We next examine how sensitive model performance is to the composition of the satellite input and the availability of spatial context. The following ablations are conducted in the end-to-end satellite embedding setting, where individual satellite components and spatial context can be selectively removed. We are unable to conduct similar experiments for AlphaEarth embeddings because that foundation model is proprietary.

When we remove Sentinel-2 imagery from the satellite data stack, we see a slight degradation in model performance across all 3 weather variables (Table A2). This indicates that much of the information relevant for micro-weather inference is already captured by the remaining satellite-derived data consisting of DEM, DSM, and land cover types. However, Sentinel-2 data does offer more granular information (e.g., vegetation density) that further boosts micro-weather inference by a small amount.

Lastly, removing spatial information from the satellite modality — i.e., only providing Sentinel-2, DSM, DEM, and land cover data at one pixel instead of in a local neighborhood — has almost no effect on the model’s ability to infer micro-scale temperature and dewpoint. However, it does increase the wind error by 5%, demonstrating that inferring micro-scale wind requires knowledge of spatially-varying surface features, not just the properties of the land surface at a specific location (Table A2).

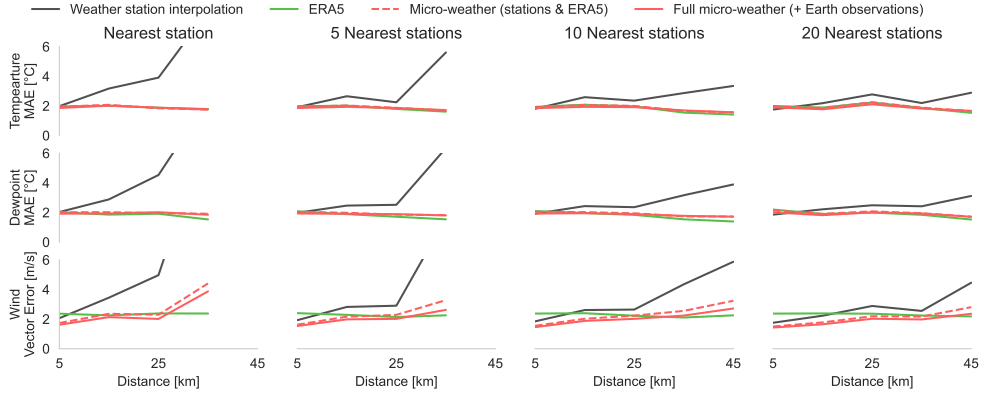


Fig. A2 Model error as a function of distance to backbone stations. Mean prediction error at held-out test stations as a function of mean distance to the k nearest backbone stations. Rows correspond to temperature, dewpoint, and wind, and columns correspond to different choices of k . Error is averaged over all hourly time steps (2020–2023) and test stations within each distance bin.

Distance to Nearest Backbone Stations

We evaluated the performance of baseline models and our full micro-weather model as a function of distance to the nearest 1, 5, 10, and 20 backbone weather stations (Figure A2). The performance of the ERA5-interpolation baseline is uncorrelated with distance to the nearest backbone weather stations, since the station modality is not directly present in ERA5 interpolation (although some stations are likely assimilated into the ERA5 product). Meanwhile, the error of the weather station-interpolation baseline is positively correlated with distance to nearest weather stations for all three variables. For the baseline model that combines ERA5 and weather stations and for our full micro-weather model, we find no correlation between nearest-station distance and performance on temperature and dewpoint prediction. However, we do see that the model achieves lower wind error on test stations with closer backbone stations. This pattern is consistent with wind being more spatially heterogeneous at the surface than temperature or humidity, and therefore more sensitive to the availability of nearby station information.

Backbone Weather Station Connectivity

We evaluate the sensitivity of model performance to backbone station connectivity by comparing the default fully connected configuration to two variants with spatially-restricted station interactions: Delaunay triangulation and 20-nearest-neighbor connectivity. We find that both variants perform worse than the fully connected configuration for temperature and dewpoint, but the differences are small (Table A3). For wind, performance is almost identical across the three specifications. This indicates that our model has limited sensitivity to the connectivity pattern; from a practical standpoint, these results suggest that when computational constraints are a consideration, restricting station connectivity may offer a reasonable trade-off between efficiency and performance.

Table A2 Baseline performance and satellite ablation comparison. Prediction errors at held-out test stations for baseline models, the micro-weather model without satellite inputs, and variants with incremental inclusion of terrain information, single-pixel Sentinel-2 imagery, full spatial context Sentinel-2, and pre-computed AlphaEarth embeddings. Temperature and dewpoint are evaluated using RMSE and MAE; wind is evaluated using vector error as well as RMSE and MAE for wind speed and wind direction. The lowest error in each column is bolded; the second-lowest error is underlined.

Model	Temperature [°C]		Dewpoint [°C]		Wind [m/s]	Wind Speed [m/s]		Wind Direction [°]	
	RMSE	MAE	RMSE	MAE	Vector Error	RMSE	MAE	RMSE	MAE
Weather Station Interpolation	4.10	2.13	3.97	2.18	2.26	2.53	1.44	80.46	61.95
ERA5	2.67	1.96	2.83	2.00	2.35	2.15	1.66	64.85	46.71
Micro-weather (stations & ERA5)	2.60	1.91	2.77	1.98	1.80	2.15	1.50	<u>66.65</u>	<u>48.68</u>
+ Terrain information (DEM, DSM, LC, etc.)	2.51	1.86	2.65	1.91	1.71	1.94	1.36	67.77	49.58
+ Single-pixel Sentinel-2	2.51	1.86	2.63	1.90	1.73	2.02	1.40	68.38	50.23
+ Spatial context Sentinel-2	<u>2.50</u>	<u>1.85</u>	<u>2.63</u>	<u>1.90</u>	<u>1.69</u>	<u>1.92</u>	<u>1.35</u>	68.17	49.84
AlphaEarth	2.49	1.84	2.64	1.89	1.67	1.86	1.29	67.62	49.45

Table A3 Sensitivity to backbone station connectivity. Prediction errors at held-out test stations for baseline models and micro-weather variants with different backbone connectivity structures, including fully connected attention, Delaunay triangulation, and 20-nearest-station connectivity. Temperature and dewpoint are evaluated using RMSE and MAE; wind is evaluated using vector error as well as RMSE and MAE for wind speed and wind direction. The lowest error in each column is bolded; the second-lowest error is underlined.

Model	Temperature [°C]		Dewpoint [°C]		Wind [m/s]	Wind Speed [m/s]		Wind Direction [°]		
	RMSE	MAE	RMSE	MAE	Vector Error	RMSE	MAE	RMSE	MAE	
Weather Station Interpolation	4.10	2.13	3.97	2.18	2.26	2.53	1.44	80.46	61.95	
ERA5	2.67	1.96	2.83	2.00	2.35	2.15	1.66	64.85	46.71	
<i>Micro-weather (end-to-end learned satellite embeddings)</i>										
Fully connected	2.50	1.85	2.63	1.90	<u>1.69</u>	1.92	1.35	68.17	49.84	
Delaunay triangulation	2.54	1.88	<u>2.65</u>	<u>1.90</u>	1.70	<u>1.92</u>	<u>1.34</u>	68.30	49.98	
20 nearest stations	<u>2.51</u>	<u>1.86</u>	2.65	1.91	1.69	1.91	1.34	<u>68.16</u>	<u>49.83</u>	

11

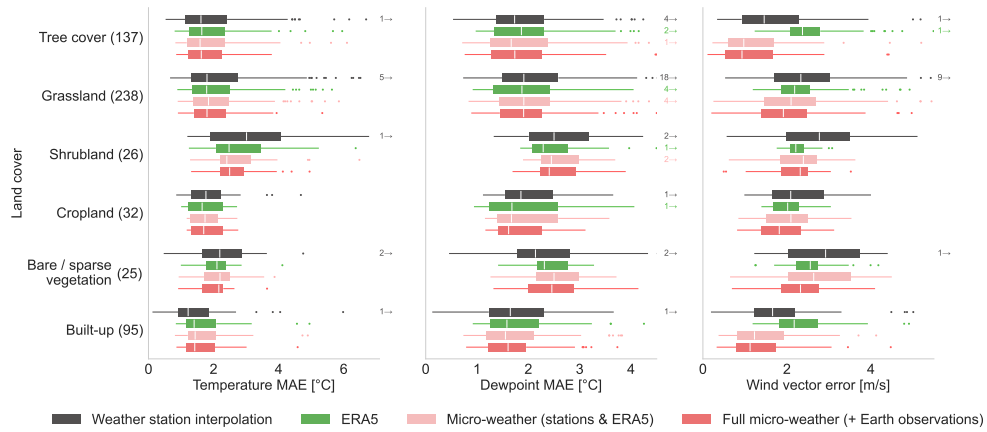
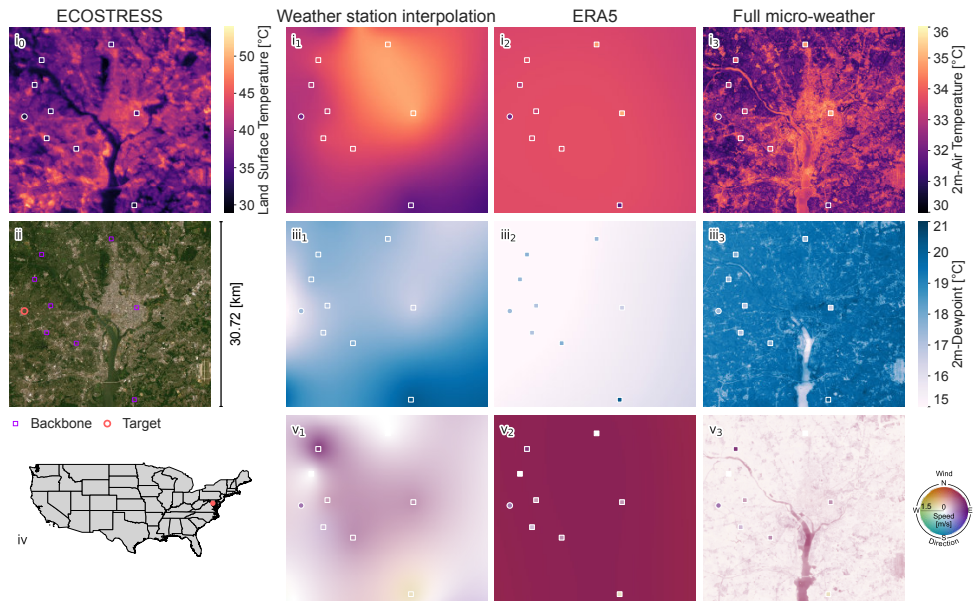


Fig. A3 Prediction error stratified by land cover type. Box plots of station-level error at held-out test stations grouped by land cover class at the station location for temperature (MAE), dewpoint (MAE), and wind (vector error). Numbers in parentheses indicate the number of test stations within each land cover class. Arrows denote the number of outliers beyond the plotted range. Models include weather station interpolation, ERA5, micro-weather (stations & ERA5), and full micro-weather with Earth observation inputs. Note that land cover classification reflects only the station pixel and does not account for surrounding land cover types.

Additional Inference Figures

Washington, D.C. (38° 53' 53.99" N, -77° 11' 6.62" W) - 2020, July 29th 20:00 UTC, 16:00 Local

a Spatial inference



b Temporal inference

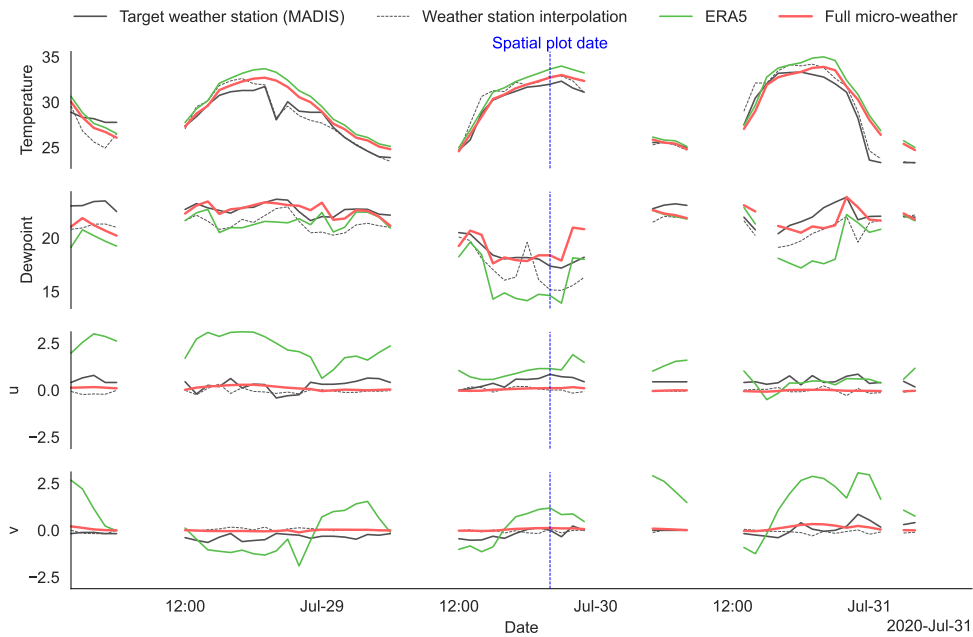
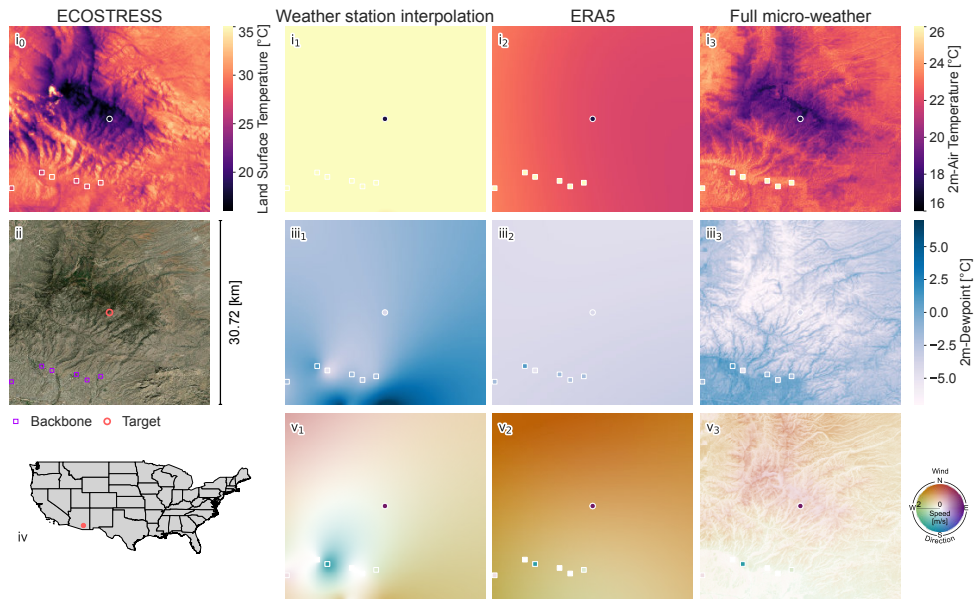


Fig. A4 Inference over Washington, D.C. Spatial inference results are shown for all three near-surface weather variables at a single snapshot, and temporal inference results are shown for a multi-day period. The blue line denotes the timestamp of the spatial inference.

Mount Lemmon, Tucson, Arizona (32° 23' 53.00" N, -110° 43' 29.99" W) - 2020, June 17th 14:00 UTC, 07:00 Local

a Spatial inference



b Temporal inference

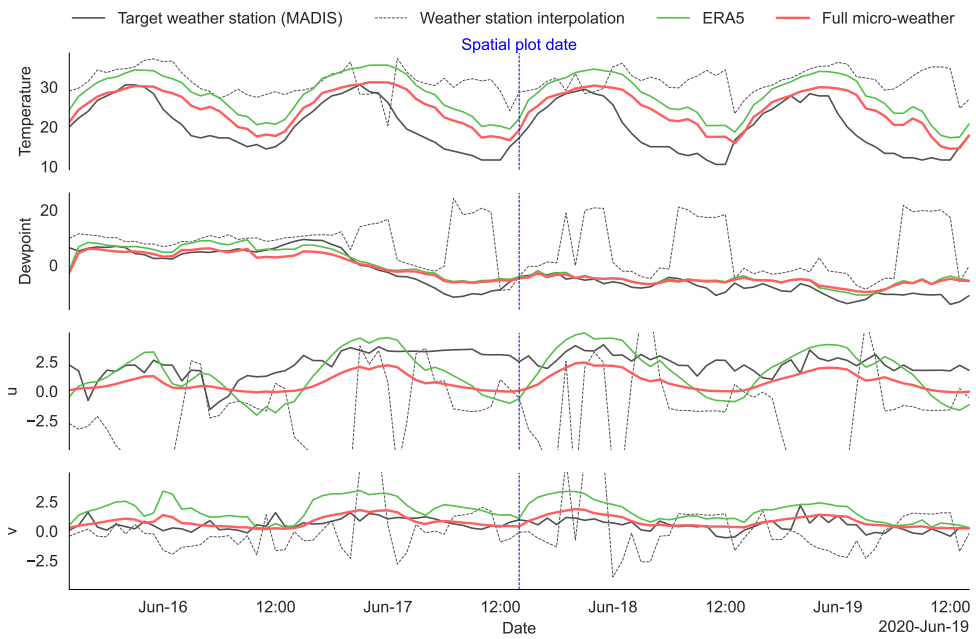
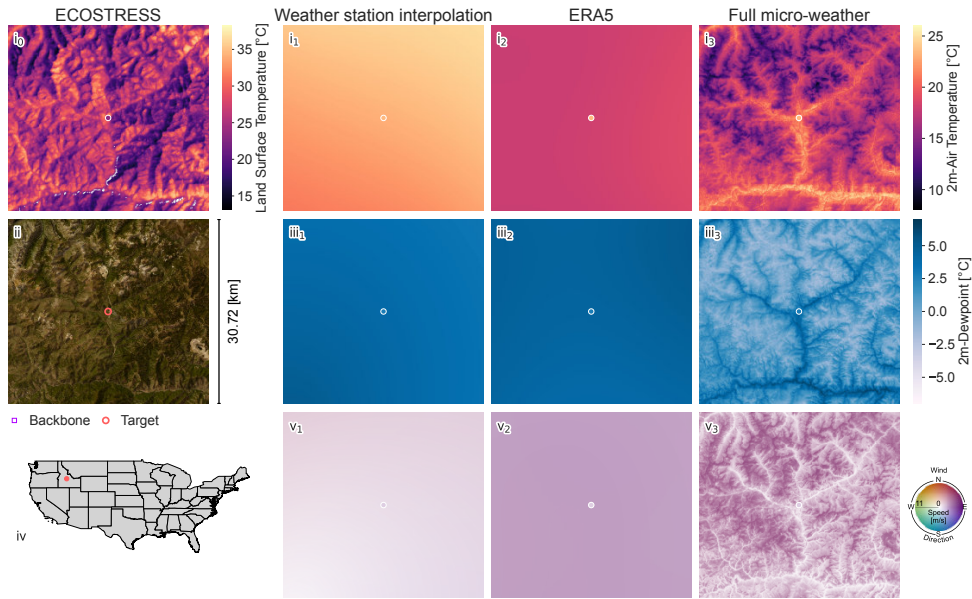


Fig. A5 Inference over Mount Lemmon, Tucson, Arizona. Spatial inference results are shown for all three near-surface weather variables at a single snapshot, and temporal inference results are shown for a multi-day period. The blue line denotes the timestamp of the spatial inference.

a Spatial inference



b Temporal inference

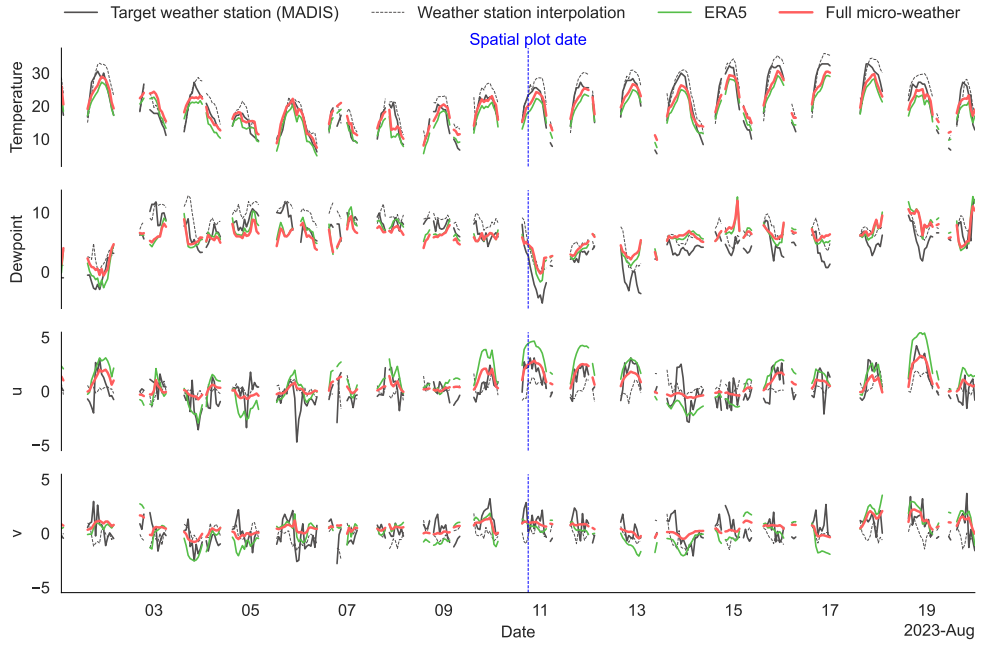
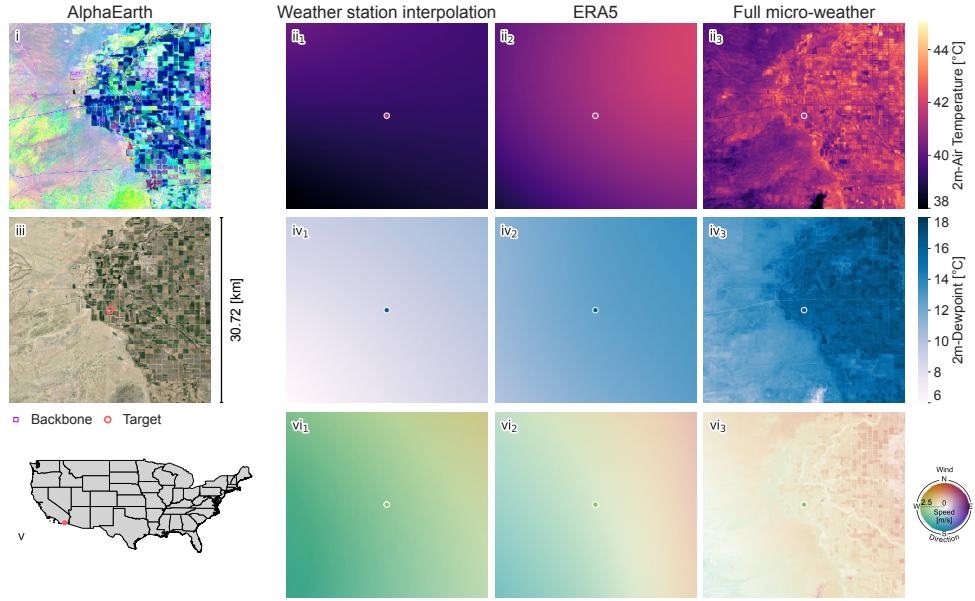


Fig. A6 Inference over Bonanza, Idaho. The weather station in Bonanza is situated at a high elevation (approximately 2,000 m above sea level) within a valley surrounded by mountains reaching up to around 3,000 m above sea level. Spatial inference results are shown for all three near-surface weather variables at a single snapshot, and temporal inference variables are shown for a multi-day period. The blue line denotes the timestamp of the spatial inference.

Calexico, California (32° 45' 32.40" N, -115° 43' 55.21" W) - 2023, August 10th 18:00 UTC, 12:00 Local

a Spatial inference



b Temporal inference

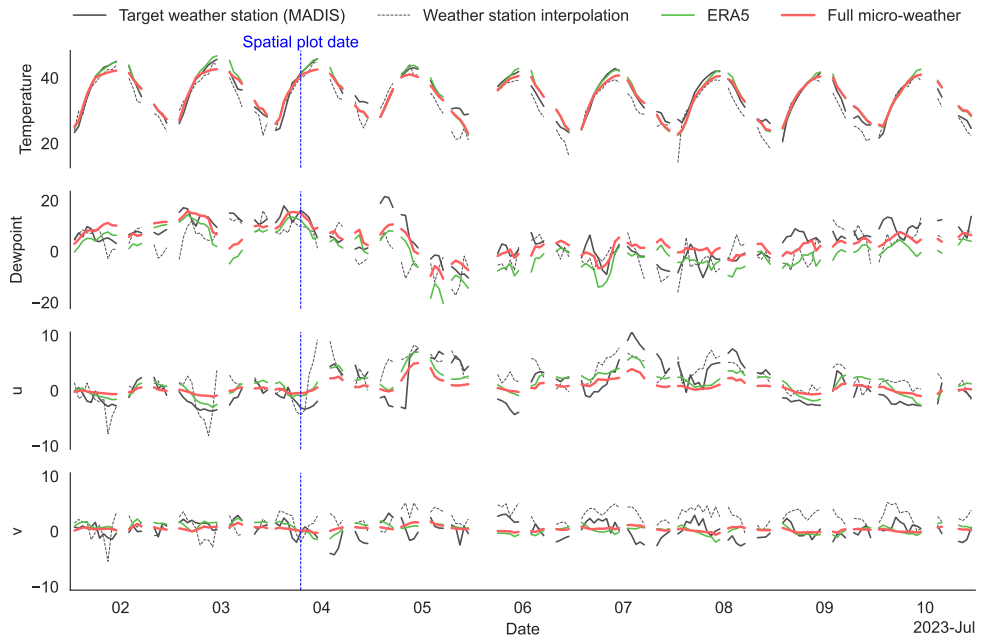
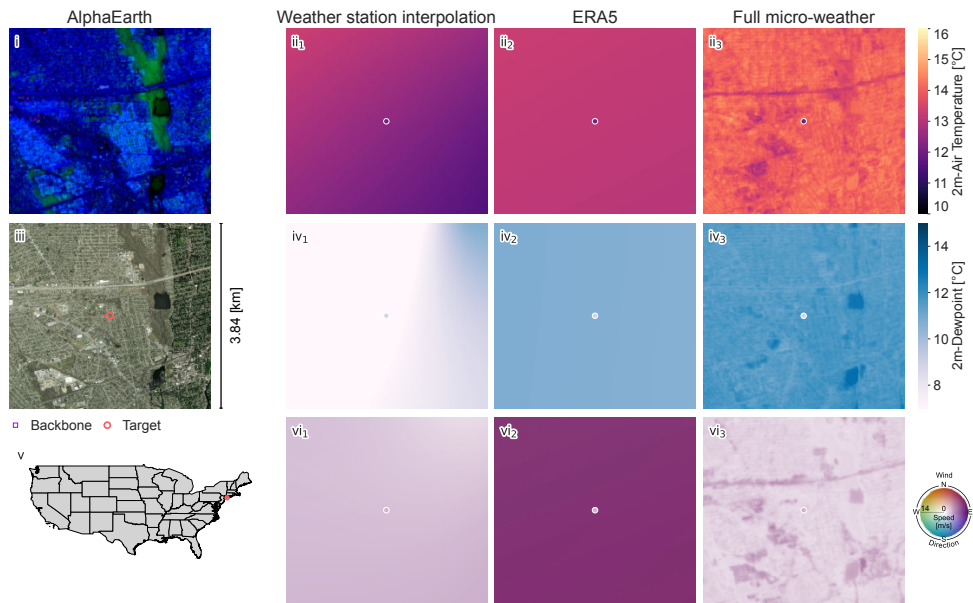


Fig. A7 Inference over Calexico, California. Spatial inference results are shown for all three near-surface weather variables at a single snapshot, and temporal inference results are shown for a multi-day period. The blue line denotes the timestamp of the spatial inference.

Long Island, NY (40° 42' 29.98" N, -73° 20' 24.62" W) - 2022, March 8th 03:00 UTC, 22:00 Local

a Spatial inference



b Temporal inference

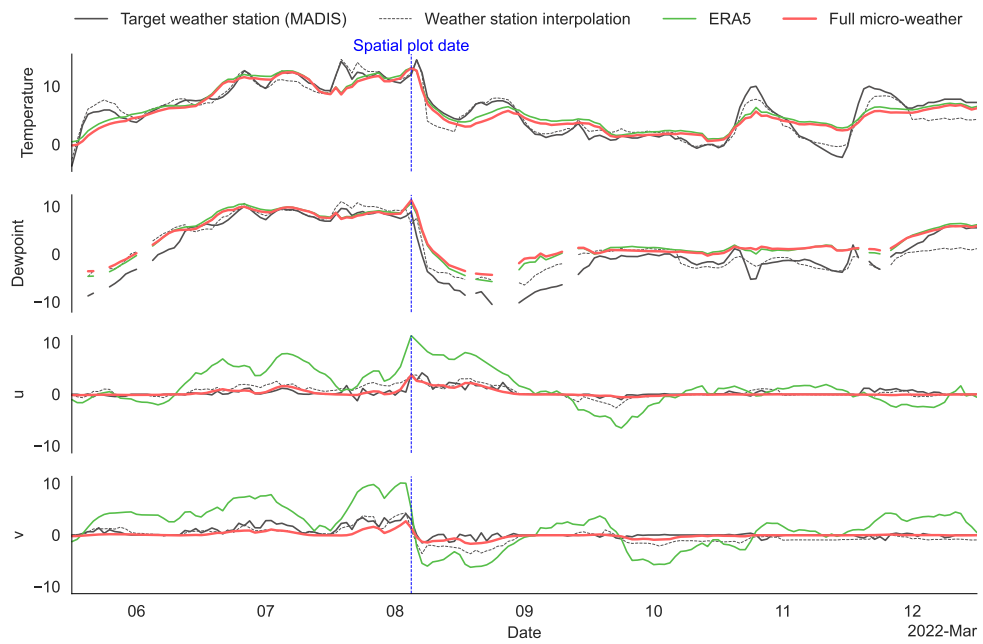
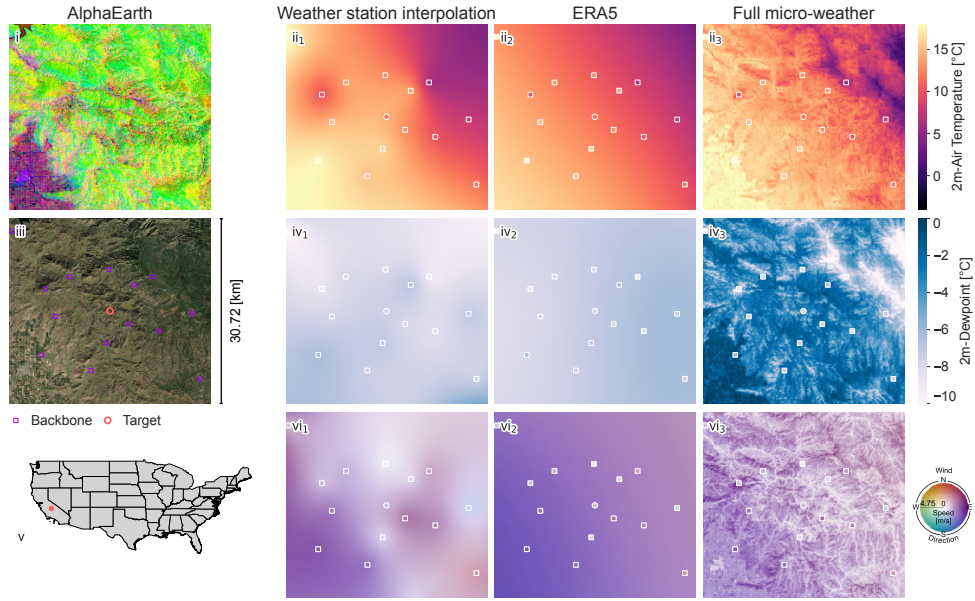


Fig. A8 Inference over Long Island, New York. Spatial inference results are shown for all three near-surface weather variables at a single snapshot, and temporal inference results are shown for a multi-day period. The blue line denotes the timestamp of the spatial inference.

Yokuts Valley, California (36° 42' 47.88" N, -119° 10' 11.99" W) - 2021, Mai 21st 03:00 UTC, May 20th, 20:00 Local

a Spatial inference



b Temporal inference

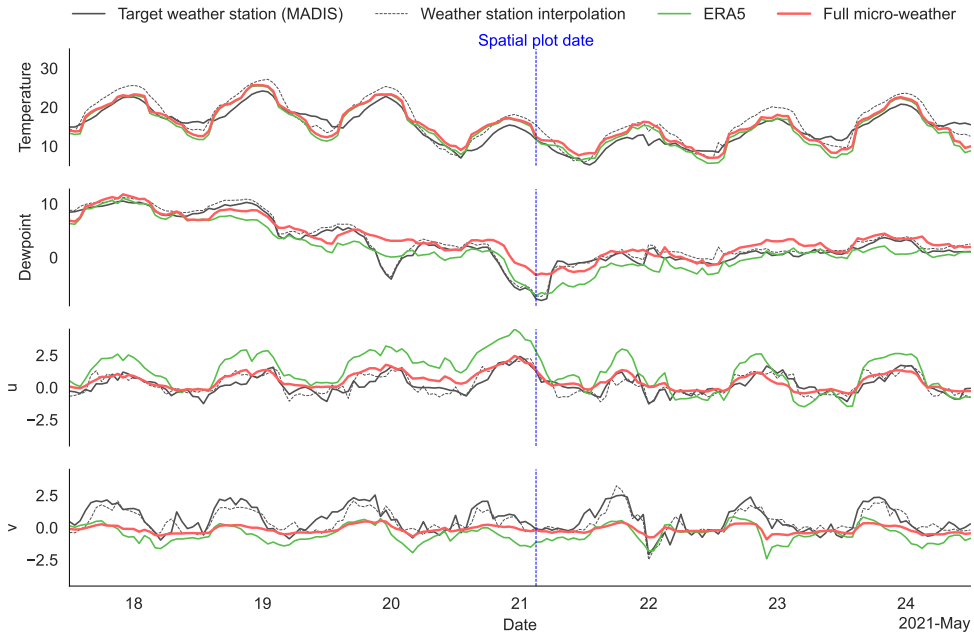
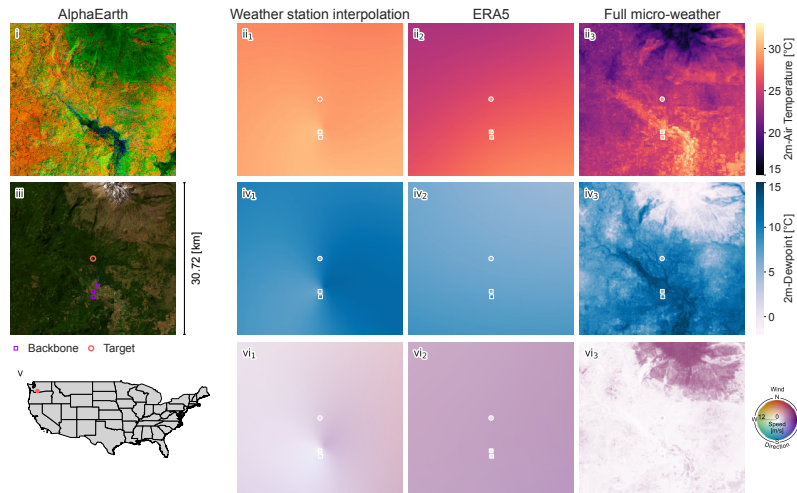


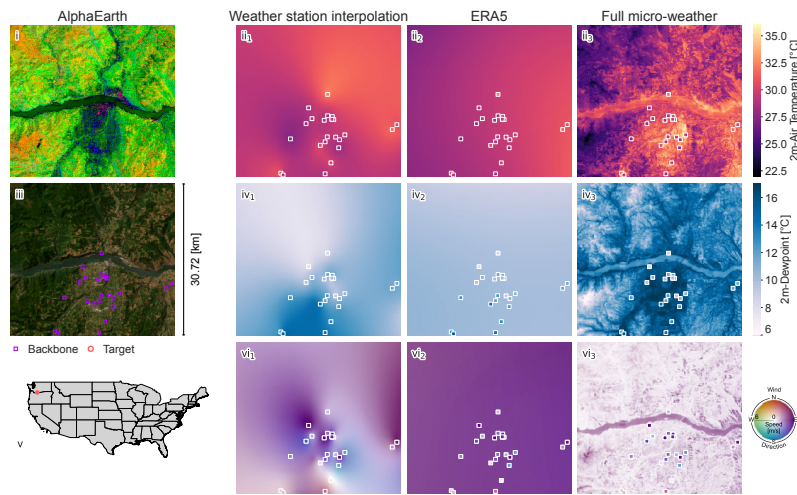
Fig. A9 Inference over Yokuts Valley, California. Spatial inference results are shown for all three near-surface weather variables at a single snapshot, and temporal inference results are shown for a multi-day period. The blue line denotes the timestamp of the spatial inference. The dewpoint spatial plot is an additional example of higher dewpoint over fields (agricultural terrain), with lower dewpoint in the mountains.

Spatial inference around Columbia River Gorge, Washington/Oregon 2022, August 03rd 23:00 UTC, 16:00 Local

a North of Columbia River Gorge (46° 3' 24.00" N, -121° 32' 19.00" W)



b Columbia River Gorge (45° 43' 7.99" N, -121° 32' 59.11" W)



c South of Columbia River Gorge, Oregon (45° 26' 49.81" N, -121° 8' 52.18" W)

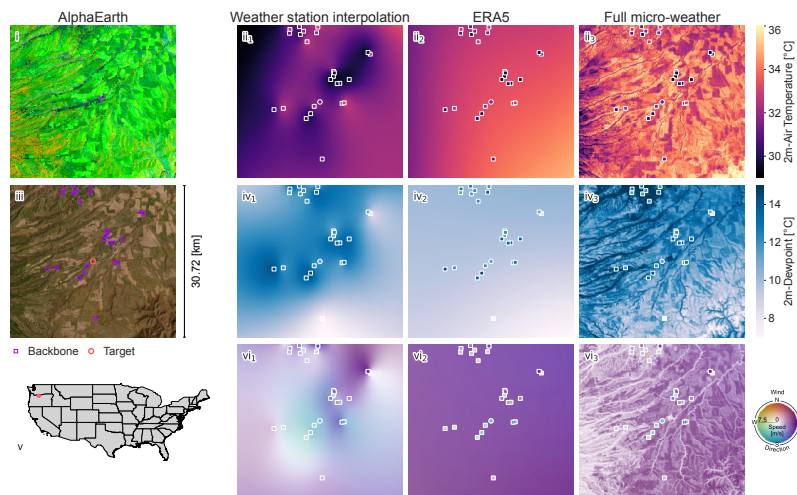


Fig. A10 Inference around Columbia River Gorge, Washington/Oregon. The area around the Columbia River Gorge is characterized by complex terrain that is known to result in wind channeling. We visualize inference in this area to assess performance in a very challenging setting. (a) The region north of the gorge includes Mount Adams. (b) Columbia River Gorge. (c) The region south of the gorge and east of the Cascade Range.

Los Angeles, CA (33° 42' 55.53" N, -117° 16' 33.07" W) - 2020, Mai 11th 21:00 UTC, 14:00 Local

Spatial inference

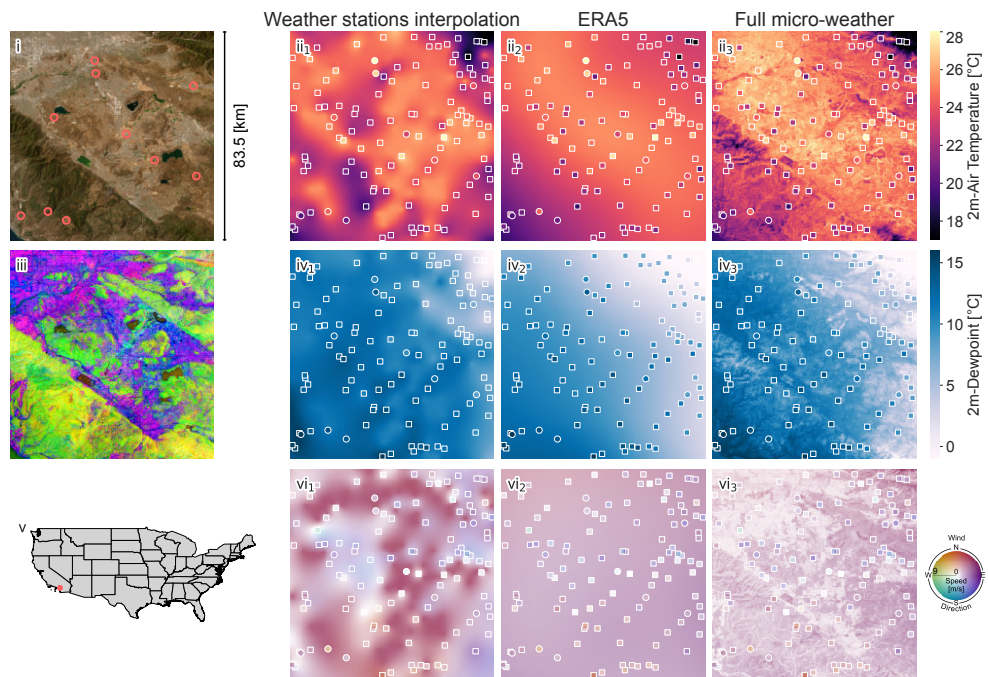


Fig. A11 Large scale inference over Los Angeles, California. The greater Los Angeles metropolitan area is the region with the densest network of weather stations in the U.S.